Universidade de Aveiro Departamento de Química
2013

João Avelãs Resende

Microstructure effects on the thermoelectric response of doped $SrTiO_3$

Universidade de Aveiro Departamento de Química
2013

João Avelãs Resende

Microstructure effects on the thermoelectric response of doped $SrTiO_3$

Efeito da microestrutura na resposta termoelétrica de $SrTiO_3$ dopado

Dissertation presented to University of Aveiro to obtain the Master degree in Materials Science, under the scientific guidance of Prof. Paula Maria Lousada Silveirinha Vilarinho, Associated Professor of the Department of Materials and Ceramics Engineering of University of Aveiro, Portugal.

Dissertação apresentada à Universidade de Aveiro para cumprimento dos requisitos necessários à obtenção do grau de Mestre em Ciência e Engenharia de Materiais, realizada sob a orientação científica da Professora Doutora Paula Maria Lousada Silveirinha Vilarinho do Departamento de Engenharia de Materiais e Cerâmica da Universidade de Aveiro

Financial support from the European Commission under the Erasmus Mundus Programme

I dedicate this work to my families, for being always my support

The board of Examiners

president

Prof. Dr. Ana Margarida Madeira Viegas de Barros Timmons
Auxiliary Professor at University of Aveiro

Prof. Dr. Vitor Brás de Sequeira Amaral
Professor at University of Aveiro

Prof. Dr. Paula Maria Lousada Silveirinha Vilarinho
Associate Professor at University of Aveiro (supervisor)

Acknowledgements

I would like to thank to my supervisor, Prof. Paula Vilarinho, for all the support and guidance during this journey.

Furthermore, I am grateful for the economical support provided by the European Masters in Materials Science scholarship 2011-2013.

I thank the technicians, Eng. Ana RIbeiro, Eng. Célia Miranda, Maria João Bastos, Mr. Octávio and Mr. Jacinto for the help in all the experimental component of the work. I thank Marta Ferro from the Microscopy Laboratory of the Department of Materials and Ceramics Engineering for her guidance and support during the Scanning Electron Microscopy sessions. I would also like to thank Pablo Diaz Chao and Prof. Emmanuel Guilmeau for the thermoelectric measurements at CRISMAT/ENSICAEN Laboratory, University of Caen, France.

In particular, I would like to thank Venkata Saravanan for all the assistance and dedication during all the work developed and principally the endless hours of discussions.

Lastly, I would like to thank my father, mother and sister who are always there for me, and all my friends, specially in Aveiro, that over this year shared important moments, leading to the conclusion of this work

keywords

Thermoelectrics, Strontium Titanate, grain size, microstructure, Seebeck effect, Electric conductivity, Thermal conductivity

abstract

Niobium doped $SrTiO_3$ ceramics were prepared with varying density and grain size in order to study the effect on the thermoelectric properties and discover a possible way to enhance the figure of merit ($ZT = S^2 .\sigma.T.\kappa^{-1}$) of this oxide. The samples were prepared by the conventional solid-state reaction technique and the grain-size variation was carried-out by the variation of precursor powders, sintering and annealing time. Structural and microstructural characterization were carried-out by XRD, electron microscopy (SEM) and optical microscope (OM). The relative density was measured by Archimedes principle, with the theoretical densities calculated from the XRD spectra. The electrical resistivity and Seebeck coefficient were measured by ZEM-3. The thermal diffusivity was measured using a Laser Flash technique and the specific heat was measure by Differential Scanning Calorimetry (DSC), in order to obtain the thermal conductivity indirectly.

The different doping compositions (5% and 20%) conjugated with the variations in density and grain size in the samples shows a potential way to improve ZT. While in the less doped samples, the higher ZT is related to the annealing time combined with larger grains and density; in the 20% Nb doped samples the smaller grain size and higher density, enhance the ZT values. The highest figure of merit obtained is 0.44 for 20% Nb doped composition, with a bimodal grain distribution. The value is the highest obtained for a Niobium doped $SrTiO_3$ ceramic.

palavras-chave

Termelétricos, titanato de estrôncio, tamanho de grão, microestrutura, efeito Seebeck, condutividade elétrica, condutividade térmica

resumo

Amostras cerâmicas de $SrTiO_3$ dopadas com Nióbio foram preparadas com diferentes densidades e tamanhos de grão, de forma a estudar o efeito sobre as propriedades termoelétricas e descobrir uma maneira possível para aumentar a sua figura de mérito ($ZT = S^2 .\sigma.T.\kappa^{-1}$). As amostras foram preparadas por reação em estado sólido convencional e a variação de dimensão de grão foi efectuada pelos variação dos pós precursores, tempo de sinterização e tempo de recozimento. A caracterização estrutural e microestrutural foram realizadas por DRX, microscopia eletrônica de varredura (MEV) e microscopia óptica (OM). A densidade foi medida pelo princípio de Arquimedes, com as densidades teóricos calculados a partir dos espectros de DRX. A resistência eléctrica e o coeficiente de Seebeck foram medidos por ZEM-3. A difusividade térmica foi medida utilizando a técnica de Flash-laser e o calor específico foi medido por Calorimetria Diferencial (DSC), com o objectivo de obter a condutividade térmica indiretamente.

As diferentes composições de dopagem (5% e 20%) conjugados com as variações na densidade e tamanho de grão nas amostras mostram uma via potencial para melhorar ZT. Enquanto que nas amostras menos dopadas, a maior ZT está relacionado com o tempo de recozimento combinado com grãos de maior dimensão e densidade; nas amostras dopadas com 20% de nióbio o menor tamanho de grão menor e maior densidade aumentam os valores da figura de mérito. O valor mais elevado da figura de mérito obtido é de 0,44 para a composição dopada com 20% de Nb e com uma distribuição bimodal de grãos. O valor é o mais elevado para um cerâmico de $SrTiO_3$ dopado com Nb.

TABLE OF CONTENTS

INDEX OF FIGURES

INDEX OF TABLES

LIST OF SYMBOLS

$E_{av}(T)$	Average energy
v_s	Average velocity of sound in the material
k_b	Boltzmann constant
q	Carrier's charge
n	Concentration of electrons
ρ	Density
ρ_{air}	Density of the air
ρ_{liq}	Density of the ethilenoglicol
ΔT	Difference of temperature
θ	Diffraction angle of the light
d	Distance between crystallographic planes
m^*	Effective mass
η	Efficiency
σ	Electric conductivity
I	Electric Current
P	Electric power
e	Electron charge
E_F	Fermi energy
ZT	Figure of merit
V_{geo}	Geometrical Volume
$\dot{Q}$	Heat rate
a, b, c	Lattice parameters
R_L	Load resistance
m	Mass
l	Mean free phonon path (MFPP)
x	Mott-Jones factor
‘	Negative charge
n	Order of diffraction

π	Peltier coefficient
$\cdot$	Positive charge
$\Delta V; \delta V$	Potential difference
R	Resistance of the thermoelectric generator
S	Seebeck coefficient
C_v	Specific heat at constant volume
c_p	Specific heat capacity
T	Temperature
β	Temperature-heating rate
K	Thermal conductance
k	Thermal conductivity
α	Thermal diffusivity
λ	Wavelength
W_{air}	Weight in air
W_{liq}	Weight in ethilenoglicol

LIST OF ABBREVIATIONS

DSC	Differential Scanning Calorimetry
GB	Grain boundary
CD	Conduction Band
GS	Grain size
RP1	Ruddlesden-Popper n=1
SEM	Scanning Electron Microscopy
STO	Strontium titanate
TE	Thermoelectric
TEG	Thermoelectric generator
XRD	X-Ray Diffraction

CHAPTER 1

Introduction

1. Introduction

1.1 Objectives

Nb doped $SrTiO_3$ ceramics have an immense importance for the future of the thermoelectric generators (TEGs). It is one of the most studied oxides for the n-type component of a thermoelectric (TE) device, due to the high power factor (PF) comparable to the state-of-the-art TE materials. However, their practical device application is hindered because of their meagre figure of merit (ZT) owing to the high thermal conductivity (κ). The modification of the microstructure has been described as one of the plausible routes to reduce the thermal conductivity and consequently, enhance of the thermoelectric properties of this material[1].

The aim of this thesis relies on understanding the effect of grain size and porosity on the thermoelectric properties of Nb doped $SrTiO_3$ ceramics. This study in bulk materials has not been reported before. For this purpose, a series of ceramics were synthesised with different composition, precursor powders distributions, sintering and annealing conditions, resulting in samples with different microstructure development.

1.2 Structure of the Thesis

The thesis is divided of 6 chapters. The 1st chapter describes the objectives and structure of the thesis. In the 2nd chapter, the concepts behind the thermoelectric phenomena and the state of the art of thermoelectric materials are presented. The 3rd chapter contains the experimental details of the work, with an additional focus on the analysis techniques used in the characterization of the prepared ceramics. In 4th chapter, the results acquired are reported, while in the 5th chapter these results are discussed through the explanation of the physical and chemical phenomena, possible relations between the different properties analysed and finally, a comparison with the literature. Lastly, broad conclusions and suggested future work are stated in the 6th chapter.

CHAPTER 2

State of the Art

2. State of the Art

Over the past decade, depleting fossil fuel reserves and increasing demand for electricity has led to an increase in research on new and alternative technologies for energy harvesting[2]. Renewable energy sources including solar, wind, tidal and geothermal have been looked up on for bridging the energy deficit, being clean energy sources from the ecological point of view. Furthermore technological advancements have led to the exploration of various novel techniques for recovering energy especially from heat. In the USA alone the energy lost in form of heat from automotive exhaustion, industrial processes and households accounts for about 60% of the total energy produced[2]. By harvesting electricity form this unused, wasted heat could significantly minimize the dependence on fossil fuel, thereby keeping carbon emission and energy cost under check[2].

The thermoelectric generators have emerged as a primary choice for harvesting energy from wasted heat[2]. In the presence of a temperature gradient across the TEGs, a percentage of the heat flow is converted in to electric energy[3] and the key for improving the output power and the efficiency is determined by the material property.

The high cost of materials combined with modest energy conversion efficiency made the application of TE generators only relevant in restrictive fields as remote power generation for unmanned systems or radioisotope thermal generators for satellites[4]. Other areas as autonomous sensors on the body and vehicles wasted heat recovery have been developed in the last years, without any further industrial application[2]. Over the last two decades, the research in the area has increased drastically due to the potential of TE materials in different configurations as large single-crystals, polycrystalline bulk materials, thin-film superlattices or ceramic oxides[5].

2.1 Thermoelectricity

The first evidence of the thermoelectric behaviour was discovered by T. J. Seebeck, in 1821[3]. He noticed the appearance of an electromotive force when a junction between two dissimilar electrical conductors was heated. This phenomenon was named the Seebeck Effect. The measurement of the voltage is performed at the ends of the wires using a galvanometer or a voltmeter. This configuration is the basis of a thermocouple, vastly used for temperature measurements. The voltage difference created by the Seebeck Effect is proportional to the intrinsic thermoelectric property of the material and the difference of temperature between the heated or cooled junction and the measurement terminals. Therefore, the Seebeck coefficient is defined as the ratio between voltage and temperature difference:

$$S = \frac{\Delta V}{\Delta T}$$

where S is the intrinsic Seebeck coefficients of the material.

In 1834, thirteen years after the discovery of the Seebeck effect, a French physicist named Jean Charles Peltier demonstrated a phenomenon that was exactly reverse of the Seebeck effect, where a current passing through a junction between two dissimilar conductors resulted in either generation or absorption of heat [3]. This phenomenon is known as the Peltier effect and it is demanding to detect since the heating generated by Joule effect is present in all metallic thermocouple junctions. In complex cases, the observation of the phenomenon is only possible by the detection of heating differences between the two electric current directions. The quantity that defines this effect is called Peltier coefficient, and relates the heat rate ($\dot{Q}$) and electric current (I) at the junction.

$$\pi = \frac{\dot{Q}}{I}$$

where $\pi$is the difference between the Peltier coefficients of the two materials.

The relation between the two effects was established through thermodynamical arguments by William Thomson, later known as by Lord Kelvin in 1855[3]. As the determination of the Peltier coefficient is complex, this relation enabled the expression of the Peltier coefficient in terms of the Seebeck coefficient, since both quantities are present

in the theory of thermoelectric energy conversion. According to Kelvin´s theory, the Peltier coefficient can be expressed in terms of the Seebeck coefficient and absolute temperature of the junction:

$$\pi = ST$$

The theory developed by Lord Kelvin demonstrated the possible existence of a third thermoelectric effect, which is called Thomson effect, explaining the reversible heating and cooling when there is a temperature gradient and electric current in a homogeneous conductor[3].

2.1.1 Physical phenomenon

The relation between electrical and thermal phenomena in the Seebeck effect is explained by the diffusion of charge carries, as electrons or holes. When a material is heated on one side, the charges carriers move from the heated zone due to the temperature difference. This condition leads to the accumulation of carriers in the cooler side, contrasting with the deficiency of carriers in the warmer side. As a result, a potential difference is created through the material. The direction of this potential difference is dependent on the type of charge carriers present in the material. In the case of metals, the presence of oppositely charged holes and electrons in comparable concentrations, leads to cancelation of this effect, resulting in a low Seebeck coefficient. However, in semiconductors, the existence of either hole or electron as majority charge carriers leads to a significant Seebeck coefficient that can be positive or negative, depending on the charge of the main carrier[3].

The origin of the thermoelectric effect can be reached through a simple classic model for metals[6]. In this case, we consider the movement of charges carriers with different average energies caused by thermal gradient, as proposed in the Figure 1.

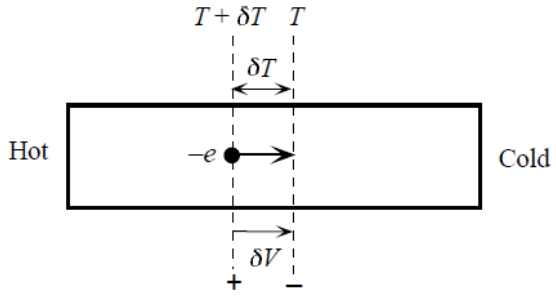

Figure 1 – Temperature gradient applied in a metal bar [6]

The potential created between two points is equal to the difference in the average energy due to thermal variations.

$$-e\delta V = E_{av}(T + \delta T) - E_{av}(T)$$

where e is the electron charge, δV is the potential difference and $E_{av}(T)$ is the average energy at T. According to the Drude model, a quantum free electrons model, the average energy can be defined as:

$$E_{av} = \frac{3}{5}\pi E_F \left[1 + \frac{5\pi^2}{12}\left(\frac{k_b T}{E_F}\right)^2\right]$$

where E_F is the Fermi energy of the material and k_b is the Boltzmann constant. The potential created and the Seebeck coefficient are defined as:

$$-e\delta V = \frac{\pi^2 {k_b}^2 T\delta T}{2E_F}$$
$$S = \frac{\delta V}{\delta T}$$
$$S = -\frac{\pi^2 {k_b}^2 T}{2eE_F}$$

Using a corrected Mott-Jones expression, the expression for metals is equal to:

$$S = -\frac{\pi^2 {k_b}^2 T}{3eE_{\mathrm{F}}}x$$

where x is a numerical factor in the "Mott-Jones thermoelectric power equation" that represents the effect of the energy dependence of electrons scattering in metals[6].

However, this model is not accurate in the case of semiconductors. The band structure provides additional considerations in the Seebeck coefficient model of semiconductors. In the kinetic definition of S, the energy difference between the average energy of the mobile carrier and the Fermi level defines the value of the Seebeck effect. In this case, with the increase of the carrier concentration, both energies - Fermi level and average energy - also increase, however, the increasing rate is different in the two cases[7]. Consequently, in a semiconductor, the S dependence with the carrier concentration is inversed. The equation that expresses the Seebeck coefficient is represented as:

$$S = \frac{8\pi^2 k_B^2}{3qh^2} m^* T \left(\frac{\pi}{3n}\right)^{\frac{2}{3}}$$

where q is the charge of the particle carrier giving the sign of the S in case of holes or electrons, m^* is the effective mass and n the concentration of the charge carriers[7]. It is important to stress that the dependence of S with the temperature is linear and increasing in absolute value.

2.1.2 Thermoelectric generator – Efficiency and Figure of Merit

The application of the Seebeck effect to the production of electricity is accomplished by a thermoelectric generator, which uses permanent temperature gradient, harvesting a part of the wasted heat[3]. A simple model of this device is represented in Figure 2.

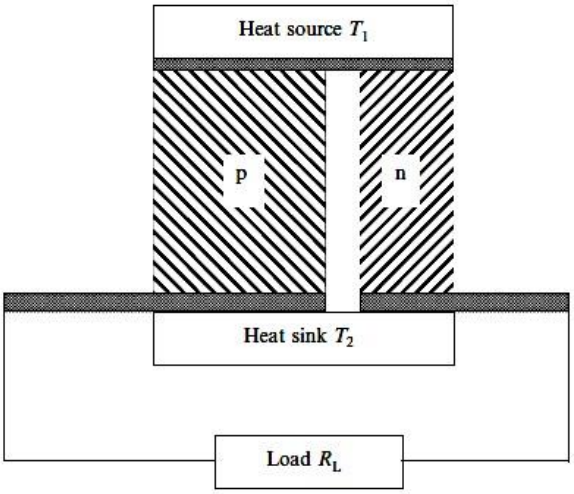

Figure 2 – Thermoelectric generator diagram[3] composed of the two branches (p and n), heat source, heat sink and external load.

In this simple model, the active region of the device is composed of two branches, each of them with a different thermoelectric behaviour. In one end of the generator, the p-type and n-type materials are in contact with each other and the heat source at a certain temperature that we consider constant in this model. On the other end of the device, each branch is connected to a common external load and maintained at a lower temperature than the heat source. This difference of temperature between the two ends produces a movement of holes and electrons from the heat source to the heat sink. Since the charge of the carries is opposite, an electric current is created. Another simple model for a refrigerator can also be formed, however, in this case, the energy is wasted in order to cool the junction region[3].

The determination of generator's efficiency is essential to recognize the conditions of possible applications, configurations and profitability. First, the power consumed in the device is spent in the load resistance.

$$P = I^2 R_L$$

where P is the power, I is the electric current and R_L is the resistance of the external load. As we consider the load and thermoelectric device in series, the current generated due to the Seebeck effect is equal to:

$$I = \frac{\Delta V}{R_L + R} = \frac{S\Delta T}{R_L + R}$$

where R is the resistance of the thermoelectric generator, considering the two different materials, and ΔT is the difference of temperature between the heat source (T_1) and the heat sink (T_2). The heat provided to the device is used to balance the heat loss due to Peltier effect at the junction and conducted along the two branches, however due to Joule effect, half of the heating returns to the source. Therefore, tree different terms are present when this configuration is considered[3].

$$\dot{Q} = IST_1 + K\Delta T - \frac{I^2R}{2}$$

where K is the thermal conductance. In this way, the efficiency of the device (η) is equal to the ratio between power consumed and heat flow out of the generator.

$$\eta = \frac{power\ delivered\ to\ the\ load}{heat\ flow\ absorbed\ at\ the\ hot\ junction}$$

$$\eta = \frac{P}{\dot{Q}} = \frac{\mathrm{I}^2R_L}{IST_1 + K\Delta T - \frac{I^2R}{2}}$$

The optimization of this value is possible by two different considerations. On one hand, the optimization of the power output is reached when the internal and external load are equal (appendix 1).

$$x = \frac{R_L}{\mathrm{R}} = 1$$

$$\eta = \frac{\Delta T}{2T_m + \Delta T + \frac{4k}{\sigma S^2}}$$

where T_m is the average temperature between T_1 and T_2, x is the ratio between load and internal resistance, k is the thermal conductivity and σ the electric conductivity. As all the internal properties of the thermoelectric materials are connected in one term, we can define:

$$Z = \frac{S^2\sigma}{k}$$

The multiplication of Z with the average temperature of the system is designated figure of merit (ZT). This adimensional factor is fundamental to evaluate the performance of the thermoelectric material, since the efficiency of a generator is fully dependent on ZT and it only concerns the material TE characteristics, consequently it is widely used to compare different materials.

In this case the efficiency can be finally written as:

$$\eta = \frac{\frac{\Delta T}{T_m}}{2 + \frac{\Delta T}{T} + \frac{4}{ZT_m}}$$

The other optimization of the system is reached by the maximization of the efficiency in order of x (appendix 2). In this case, the final efficiency expression is the following:

$$\eta = \frac{\Delta T}{T_1} \quad \frac{\sqrt{1 + \mathrm{ZT_m}} - 1}{\sqrt{1 + \mathrm{ZT_m}} + \frac{\mathrm{T_2}}{\mathrm{T_1}}}$$

Once again, the efficiency is dependent on ZT, with a direct relation. As ZT tends to infinity, the efficiency reaches the Carnot cycle limit for thermal machines, providing the maximum and impossible limit of this device. The plot of the efficiency relation with temperature and respectively ZT is present in Figure 3.

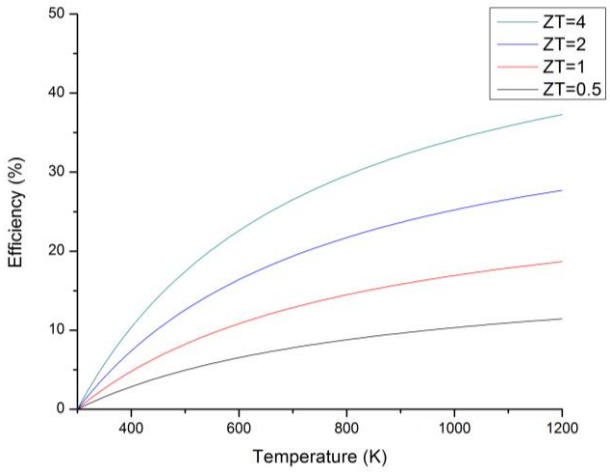

Figure 3 –Thermoelectric efficiency vs the heat source temperature for different ZT values

As visible in the figure, the efficiency of a TEG depends on the value of Z, which is an intrinsic property of the material and the temperature difference across it. Consequently, if at high temperatures (1000K) a ZT of 1 is enough to obtain an efficiency of 15%, the same efficiency value at 500 K can be obtained[8] if the ZT of the material is ~ 4.

2.1.3 Electric and Thermal conductivity

In order to realize high value of ZT in a material, it is essential to have *k* as low as possible while having a high value of power factor (PF=$S^2\,\sigma$)[7]. Therefore, the study of these properties changes is fundamental to understand how the efficiency of the device can be increased.

A high electrical conductivity, to promote the electrical flow of charge carriers, and a low thermal conductivity, to decrease the heat loss in the device, are essential characteristics for the electric generator. In semiconductors, the electrical conductivity is determined by the concentration of charge carriers (n) and its mobility (μ).

$$\sigma = qn\mu$$

where q is the charge of the carrier. Contrarily to the Seebeck coefficient, the high concentration of charge carriers improves the conduction of the material[3].

The thermal conductivity can be separated in two different parts, electronic (k_e) and phononic (k_L) conduction.

$$k = k_L + k_e$$

The first contribution comes from the electrons ability to transfer heat. According to the Wiedemann–Frenz Law, this term is fairly dependent of the electrical conductivity and can be expressed as:

$$k_e = L\sigma T$$

where L is the Lorenz factor (2.4×10^{-8} $J^2.K^{-2}.C^{-2}$). In the high temperature case, this term increases linearly with the temperature. Nevertheless, the thermal conduction is overruled by the phonon term that can be expressed as:

$$k_L = \frac{1}{3} C_v \, l \, v_s$$

where C_v is the specific heat at constant volume, l is mean free of phonon path (MFPP), and v_s is the average velocity of sound in the material[9]. Analysing the equation, it is possible to infer that a reduction of the MFPP, also leads to k_L decrease. A nanostructured material or a crystal with a super-lattice structure can be two possible ways to achieve a reduction of the thermal conductivity due to an increase of the phonon scattering and reduction of phonons spectrum[3,9].

2.2 Thermoelectric materials

Since the 1950s, the thermoelectric materials progress has increased due to the first well-established materials developed in this decade. The first generation of materials include the Bi_2Te_3, PbTe and SiGe as bulk materials, which were designed to be applied at room, intermediary and high temperature, respectively, exhibiting a figure of merit below 1[10]. In the following decade, the main ambition was the enhancement of the figure of merit by controlled doping and solid solutions such as Bi_2Te_3–Sb_2Te_3, PbTe–SnTe, and $Si_{1-x}Ge_x$. Until the 1990s, the research intensity has decreased worldwide and the best alloy family of materials was $(Bi_{1-x}Sb_x)_2(Se_{1-y}Te_y)_3$ with ZT values around 1[10].

In the last two decades, the energy problems worldwide lead to the reappearance of research on thermoelectrics as a support technology for power generation and cooling applications. This revival research was motivated by the need to develop high-performance

themoelectrics using new families of bulk thermoelectric materials and synthesizing low-dimensional thermoelectric materials systems. The study of a variety of materials has been intensified with a special highlight in Bi_2Se_3, Sb_2Te_3, $PbTe_{1-x}Se_x$, TAGS (TeAgGeSb), LAST (PbAgSbTe) and Half-Heusler alloys (NbCoSn, TiNiSn, HfNiSn)[11], as observed in the Figure 4. Different strategies such as "Phonon-gas electron-crystal" materials, or nanostructured materials with the production of superlattices, quantum dots, nanowires, and nanocomposite lead to drastic improvements of the ZT, reaching the record value of 2.2 for bulk materials of PbTe endotaxially nanostructured with SrTe and 2.4 for thin films of Bi_2Te_3/Sb_2Te_3 [10-13].

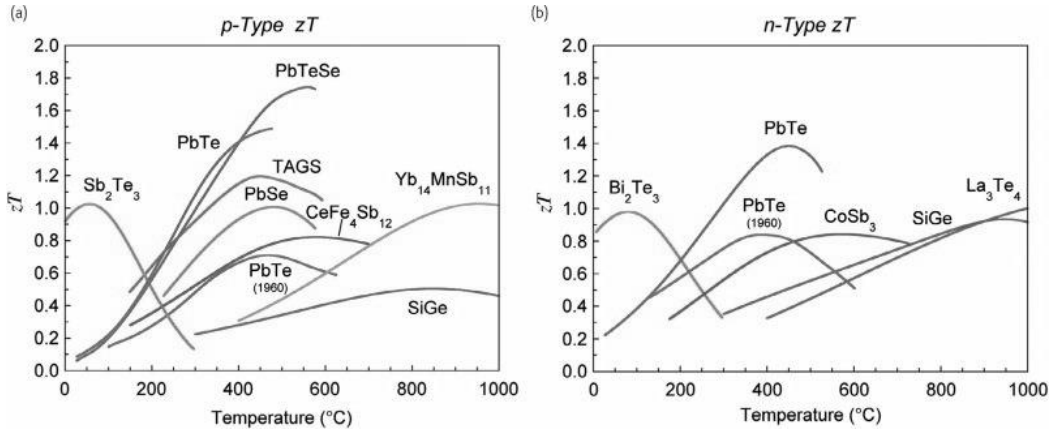

Figure 4 – Thermoelectric performance of the state-of-the-art materials[11]

The implementation of this technology is currently broader than in the early years, when the main application was for spatial devices. In the automobile industry, some companies as BMW, Honda, Porsche, Nissan and General Motors have been researching for the implementation of this technology in cars and even some of them have already developed prototypes[8]. The BMW latest produced model - BMW X6 – can generate 600 W, nevertheless, the final goal of 1000 W for the implementation in mass production has not yet achieved[8]. Additionally, biomedical applications are emerging, in order to create electrically autonomous devices to be implanted in the body[14]. Different formulations are appearing as generator wristbands on the microwatt range[14], or even pacemakers that recharge with the body warm[15].

However, a multiplicity of problems surfaces related with the toxicity of some materials as lead, scarcity of elements, low stability at high temperatures and use of heavy elements[8], hindering the technological implementation.

2.2.1 Thermoelectric Oxides

Thermoeletric oxides are expected to overcome the shortcoming of the conventional TE materials not only due their excellent transport property (when suitably doped) and high temperature stability due to the high melting points, but also owing to their cost effectiveness, natural abundance and non-toxic nature. In this case, oxides will have more importance in the generation of energy, than in the refrigerator technology, since there are already more capable materials for the cooling regime than oxides.

1.1.1.1 P-type oxides

In the p-type semiconductor, the $Ca_3Co_4O_9$ and the Na_xCoO_2 are the most researched materials, showing higher values of ZT (from 0.5 to 1). All these materials have the Co^{3+} ion that allows the increase of the Seebeck coefficient due to spin characteristics[16]. Furthermore, the structure of these materials enhance the thermoelectric properties, since the Na_xCoO_2 presents alternated layers of Na and CoO_2 (Figure 5) responsible for the reduction of the thermal conductivity due to phonon scattering increasing. The integration of dopants also increases the ZT, where the Au, Sr, K and Nd are the most used elements[16].

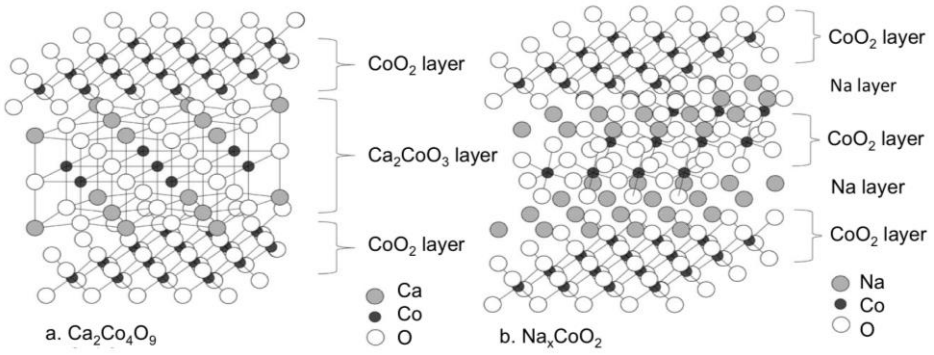

Figure 5- Structure of $Ca_3Co_4O_9$ and the Na_xCoO_2[16]

The study of other materials is also reported in the literature, as $LaCoO_3$, $LaCuO_4$ or $CuAlO_2$[16]; however with lower ZT values when compared with $Ca_3Co_4O_9$ and the Na_xCoO_2.

1.1.1.2 N-type oxides

The n-type semiconductors, in general have demonstrated lower values of ZT when compared with their p-type counterpart. There are three relevant n-type materials in the development of thermoelectric devices: $CaMnO_3$, ZnO and $SrTiO_3$[16]. The first one presents values of ZT around 0,3 when doped with Yb or Nb. Zinc oxide exhibits some opportunities different from the others, due to the possible configuration as nanowires. In bulk, when doped with Ni, In, Ga and the most used Al, ZnO exhibits ZT values around 0,6, presenting strong grain size dependence. Nevertheless in nanowires, these values can be improved by one order of magnitude since the thermoelectric properties as Seebeck coefficient and electric conductivity increase drastically[16]. However, the understanding of the phenomena is yet to be completed. The last material, $SrTiO_3$ has been highly studied, showing values of ZT around 0,37 [17] and it is the chosen material in this research.

Moreover, a thermoelectric device only with oxides, providing output power around 500 mW has been already produced[18]. The structure is composed of $Ca_3Co_4O_9$ as p-type material and ZnO doped with In_2O_3 for the n-type branch. This device operates with a difference of temperature between room temperature and 1100 K, which confirms the possibility of using oxides in high temperature regimes. The current situation in this family of materials can be resumed in the next figure[16].

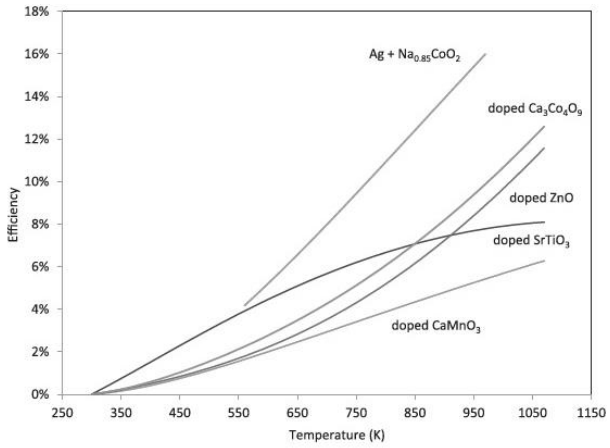

Figure 6- Possible efficiency of most studied thermoelectric oxides, n-type and p-type[16]

2.3 Strontium titanate - $SrTiO_3$

2.3.1 Bulk material

Strontium titanate ($SrTiO_3$ – STO) is an insulator material, with a band gap of 3.2 eV and a density (ρ) of 5,12 g/cm^3 [19]. It presents a cubic perovskite structure of the ABO_3-type (Figure 7) above 105 K ($Pm\bar{3}m$) with a lattice parameter of a = 0,3904 nm, where the A cations (Sr^{2+}) are situated at the cube corners, the small B cations (Ti^{4+}) at the body centre and oxygen ions at the face centres[20]. This chemical-structure offers to the material a very high melting point, around 2080 ºC, which indicates its potential for high temperatures applications[20]. The stability of this perovskite structure is connected with the relation between ionic radii of the cations and anions and the high degree of ionic bonding[21].

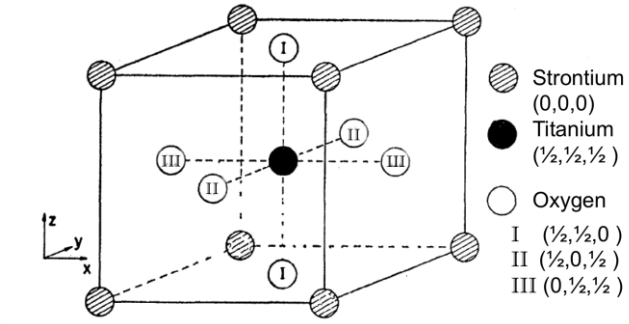

Figure 7 - The crystal structure of strontium titanate[22]

The intensive research on this material is explained by the fundamental characteristics discovered in the last fifty years that include the semiconductor behaviour when doped or with an high concentration of oxygen vacancies[19], superconductivity below 0,25 K[23], structural phase transition[24] and quantum paraelectric behaviour below 4 K with a very high dielectric constant[25].

These properties made $SrTiO_3$ based compounds appropriate for different electroceramic applications. The high dielectric constant and low dielectric loss enables the application in layer capacitors, varistors, sensors and other electronic devices[26,27]. Presently, the integration in devices for military, airport and police radars, satellite communication systems, mobile phones and wireless computer networks is already established, because of its importance in microwave microelectronic elements[28].

Additionally, the integration and miniaturization of devices requires high reliability, small sizes and high capacitance capacitors that can be processed by different synthesis methods, depending on the final application[27]. $SrTiO_3$ can be produced by a variety of processes that includes conventional mixture of oxides, microwave synthesis, coprecipitation, hydrothermal synthesis, alkoxide hydrolysis, and metallo-organic processing[26].

2.3.2 Thermoelectric Applications

$SrTiO_3$ is one of the promising oxides materials for the n-type component of a TEG. The intrinsic high Seebeck coefficient, the large electrical conductivity in doped systems and the high melting temperature are fundamental properties of this material for TE application[17]. The electronic band structure of the material is the central explanation for the exhibited Seebeck coefficient. The conduction band is formed by Ti 3d orbitals triply degenerate and the valence band is formed by an O 2p orbital, resulting in a material with a band gap of 3.2 eV[1]. The effective mass of the electrons in the conduction band (CB) is quite large (m^*_e=1,16~10 m_0) due to the nature of the d-band. This high effective mass is the main reason for the large Seebeck effect present in STO, even with a high concentration of electrons in the CB[1]. In $SrTiO_3$, single crystal the values of S range from -108 $\mu V.K^{-1}$ at room temperature to -500 $\mu V.K^{-1}$ at 1000K[17,29].

Consequently, due to the high electron conduction when doped combined with a large Seebeck coefficient, the thermoelectric power ($S^2\sigma$) is high enough to be considered as an opportunity for thermoelectric applications[1].

1.1.1.3 Doped systems of Strontium titanate

The insulator behaviour of $SrTiO_3$ inhibits the application as a thermoelectric of undoped material. However, since the tolerance for doping is relatively high, the doping of this material with different elements in the A (Sr) or B (Ti) site can provide enough charge carriers to enhance the conductivity of the material[1]. The different possible dopants ranges from La[30-35], Ca[36], Y[37], Dy[38], Nd[31,39], Ta[40], W[40], Yb[32] and Eu[41] for the A site, replacing Sr in the structure and Nb [17,33,36,40-45] for the B site, replacing Ti cations in the structure. The high solubility of dopants in the STO structure enables the creation of bulk ceramics with

20% of Nb or La and thin films with 40% of Nb doping [17], providing high concentration of charge carriers. The ZT values of these doped systems are currently in the order of 0,37 at 1000 K, in the best case of 20% Nb doped epitaxial film and similar results for ceramics [17,42]. However, these values are low for practical application of $SrTiO_3$; nevertheless it shows the relevance and potential of this material for thermoelectric applications. These values are possible as a result of the combination of high electric conductivity values (250 $S.cm^{-1}$) with low thermal conductivity (3,5 $Wm^{-1}K^{-1}$)[42]. Doping in the Sr site state has been less successful, with ZT values at 1000 K varying from 0,087 to Eu[41], 0,2 to Yb[32], 0,25 to Dy[38], 0,28 to Nd[39] and 0,37 to La[35] doping. The comparison of the ZT values for two dopants, La and Nb is present in Figure 8.

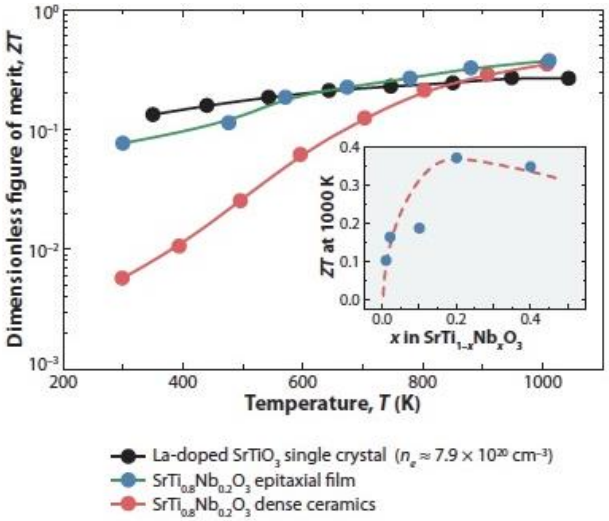

Figure 8 - Figure of Merit for most appropriate dopants (La and Nb)[1]

1.1.1.4 Defects chemistry – Donor doping

A study on the defects chemistry of the $SrTiO_3$ based materials is fundamental to understand the mechanisms that allow the creation of high conductive bulk ceramics. The reactions equations that present electric conduction fundaments follow the Kröger-Vink notation[46].

In the undoped case, the ionic point defects in the perovskite structure are dominated by vacancies formation than interstitials ions. The oxygen vacancies ($V_O^{\bullet\bullet}$) formed are compensated by strontium vacancies (V_{Sr}'')[46]. In this case, a partial Schottky reaction is favoured in comparison with other Frenkel reactions:

$$\mathrm{Sr}_{\mathrm{Sr}}^{x} + O_O^x \rightarrow V_{Sr}'' + V_{\ddot{O}} + SrO$$

This mechanism is one of the possible processes for the creation of the Ruddlesden-Popper phases. Furthermore, the atmosphere equilibrium of the surrounding environment also controls the concentration of point defects. At low pressure of oxygen, the creation of oxygen vacancies will be a dominant mechanism, contributing for the increase of electrons concentration.

$$\text{null} \rightarrow V_{\ddot{O}} + 2e' + \frac{1}{2}O_2$$

Additionally, the generation of pairs of electrons and holes is other intrinsic defect reaction cause by thermal excitation across the band gap.

$$null \rightarrow \ e' + h^{\cdot}$$

All of these three reactions have a mass action law associated that determines the concentration of each species. The electroneutrality equation can also be determined in this case.

$$K_s = [V_{Sr}''][V_{\ddot{O}}] = K_s^0(T)\exp\left(-\frac{E_s}{k_b T}\right)$$

$$K_{Red} = n^2\,[V_{\ddot{O}}]\,P(O_2)^{\frac{1}{2}} = K_{Red}^0\exp\left(-\frac{\Delta H_{Red}}{k_b T}\right)$$

$$K_i = n\,p = K_i^0\exp\left(-\frac{E_B}{k_b T}\right)$$

$$n + 2[V_{Sr}''] = \mathrm{p} + 2[V_{\ddot{O}}]$$

where K_s is the reaction coefficient of the Schottky defects, K_{Red} of the reduction, and K_i of the electron-hole creation.

The addition of donor ions to the composition of the material can change the creation mechanisms of intrinsic defects. The following considerations are valid in a fixed concentration of donors model, with variation of oxygen pressure and temperature. In this case, we consider donors with a +5 valence, niobium ions for instance, in the B site (Ti^{+4}) to study the possible defect's creation. One possible mechanism for the compensation of

the dopant positive charge is the creation of Sr vacancies, as the Ti vacancies are unfavourable to be generated[47].

$$\frac{x}{2}Nb_2O_5 + SrO + (1-x)TiO_2 \rightarrow \left(1-\frac{x}{2}\right)Sr_{Sr}^{x} + \frac{x}{2}V_{Sr}'' + xNb_{Ti}^{\cdot} + Ti_{Ti}^{x} + 3O_O^x + \frac{x}{2}SrO$$

The starting composition can be adjusted in order to prevent the formation of SrO by reducing the amount by $\frac{x}{2}$. As the ion behaves as a positive charge in the B site, we reach a new electroneutrality condition:

$$n + 2[V_{Sr}''] = \mathrm{p} + 2[V_O^{\cdot\cdot}] + [Nb_{Ti}^{\cdot}]$$

Depending on the oxygen pressure, the electroneutrality equation can be approximated by different ways. In a highly reductive atmosphere, the creation of oxygen vacancies mechanism will control the defect formation, so the concentration of electrons will compensate the oxygen vacancies:

$$n = 2[V_O^{\cdot\cdot}]$$

In this case, we can obtain the value for the concentration of electrons only dependent on the oxygen partial pressure and K_{Red}

$$n = (2K_{Red}(T))^{1/3}\, P(O_2)^{-1/6}$$

In this case, the reduction of the electrons and oxygen vacancies is proportional to $P(O_2)^{-1/6}$, opposite to the situation with the holes and strontium vacancies, where the increase is proportional to $P(O_2)^{1/6}$.

As the oxygen pressure increases, the concentration on electrons and oxygen vacancies decreases, until the concentration of electrons is similar to the amount of donor introduced in the system. This situation gives a new condition for the electroneutrality that dominates the system until higher oxygen pressures.

$$n = [Nb_{Ti}^{\cdot}]$$

In this second regime, the concentration of electrons is constant and equal to the concentration of dopant; the oxygen vacancies are reduced with the increase of the oxygen partial pressure ($P(O_2)^{-1/2}$); the vacancies of strontium increase proportional to $P(O_2)^{1/2}$, and the holes concentration are kept constant as the electrons concentration.

In a third regime where the oxygen partial pressure is higher, the electroneutrality equation is again reconsidered. When the vacancies of strontium reach values similar to the concentration of dopant, the negative compensation is no longer done by the electrons but by these ionic vacancies.

$$2[V_{Sr}^{''}] = [Nb_{Ti}^{\cdot}]$$

In this case, the both ionic vacancies are maintained constant, contrasting with the concentration of electron that decreases proportional to $P(O_2)^{-1/4}$ and the holes concentration that increases proportional to $P(O_2)^{1/4}$. The corresponding Kröger-Vink diagram of these three situations at 1000 ºC is presented in the Figure 9.

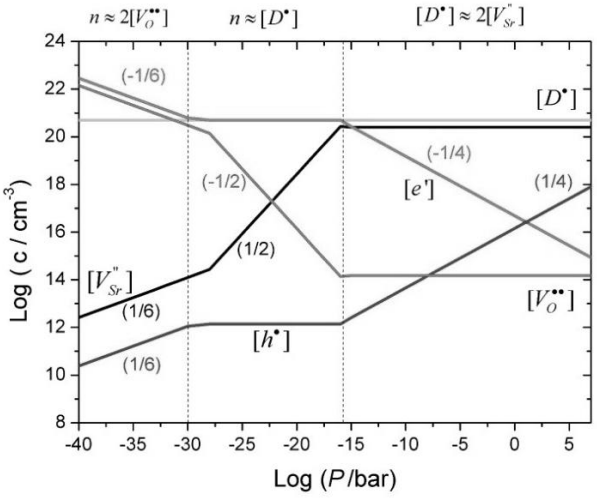

Figure 9 - Kröger-Vink diagram for 3at% donor doped $SrTiO_3$ at 1000°C[46]

Other possible mechanism for the increasing of the electrons concentration in the STO structure is through the modification of the oxidation state of Ti ions[47]. In this situation, the insertion of a donor ion in the material will be compensated by the reduction of Ti.

$$\frac{x}{2}Nb_2O_5 + SrO + (1-x)TiO_2 \rightarrow Sr_{Sr}^{x} + xNb_{Ti}^{\cdot} + xTi_{Ti}^{\prime} + (1-x)Ti_{Ti}^{x} + 3O_O^{x} + \frac{x}{4}O_2$$

The electroneutrality equation is altered in this case, being the Ti^{3+} ions counted as negative charges.

$$n + [Ti_{Ti}^{\prime}] = \mathrm{p} + 2[V_O^{\cdot\cdot}] + [Nb_{Ti}^{\cdot}]$$

As in the strontium vacancies, similar considerations can be assume in this case, in order to understand the defects dependence with the oxygen pressure.

1.1.1.5 Ruddlesden-Popper Structures

The $SrTiO_3$ presents other important characteristic that can be obtained in the production, reduction treatments or the doping of the material, which might be a possible solution for the improvement of the thermoelectric properties. The natural superlattices of the Ruddlesden-Popper phases in the perosvkite structure $SrO(SrTiO_3)_n$ (n = 1, 2) are composed of alternatively stacked n-layer of $SrTiO_3$ blocks and one layer of SrO, where the n equal to infinite corresponds to the pure $SrTiO_3$ case[48]. The image of this situation is shown in the next figure.

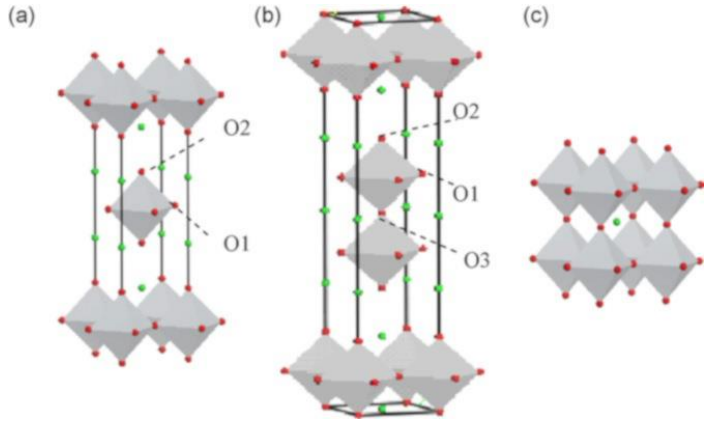

Figure 10 -Ruddlesden Popper structures: a) RP1, b) RP2, c) RP∞=STO[49]

The formation of the different RP structures is controlled by the defects and stoichiometry in the fabrication of the material, as seen in Figure 11.

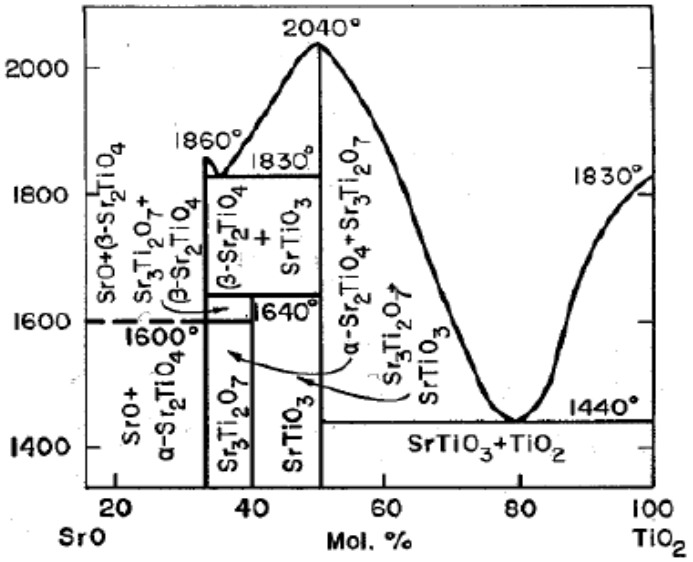

Figure 11 - Phase diagram of TiO_2-SrO[50]

This family of compounds can reduce the thermal conductivity due to the enhancement of phonon scattering at the interfaces of $SrO/(SrTiO_3)_n$ preserving the transport properties and Seebeck effect in the perovskite layers. The stability of the RP phases allows additionally the synthesis of dopant into the structure as Nb, Nd or La[31,43,48,51]. The effects on the other thermoelectric properties also appear with a decreasing of Seebeck effect and electrons conduction[1]. The Figure 12 shows the reduction of thermal conductivity of these structures (RP2) when compared with doped $SrTiO_3$, and the figure of merit that shows lower values when compared with the state of the art $SrTiO_3$ possibilities.

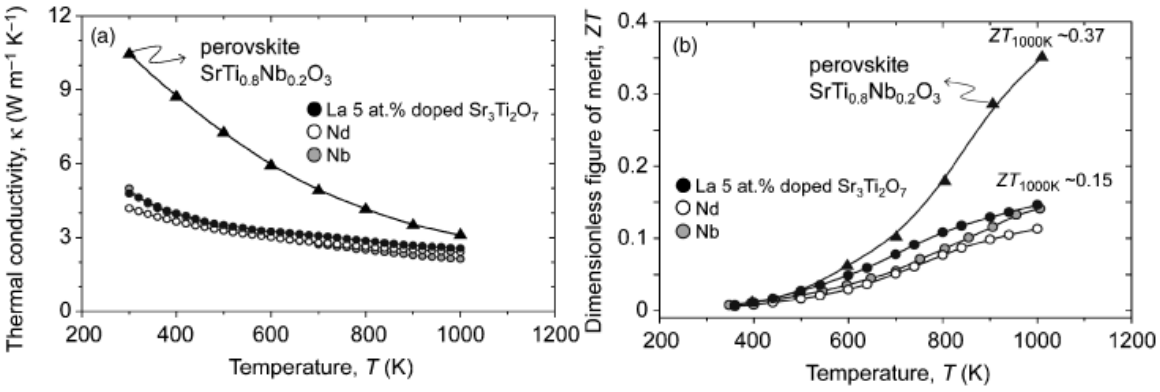

Figure 12- Thermal and ZT results of RP2 structures doped with La, Nd and Nb[48]

The defect chemistry of these structures can be defined by the creation of Sr vacancies or changes in the Ti oxidation state, as in the $SrTiO_3$ case.

$$n\frac{x}{2}Nb_2O_5 + (n+1)SrO + n(1-x)TiO_2 \rightarrow$$

$$\rightarrow n\,Sr_{Sr}^{x} + n\,xNb_{Ti}^{\cdot} + n\,xTi_{Ti}^{\prime} + n\,(1-x)Ti_{Ti}^{x} + n\,3O_{O}^{x} + \frac{x}{4}O_2 + SrO$$

or:

$$n\frac{x}{2}Nb_2O_5 + (n+1)SrO + n\,(1-x)TiO_2 \rightarrow$$

$$\rightarrow n\left(1-\frac{x}{2}\right)Sr_{Sr}^{x} + n\frac{x}{2}V_{Sr}^{\prime\prime} + n\,xNb_{Ti}^{\cdot} + n\,Ti_{Ti}^{x} + n\,3O_{O}^{x} + \left(n+\frac{x}{2}\right)SrO$$

1.1.1.6 Grain size effect on the thermoelectric properties

As discussed before, the control of the grain size in $SrTiO_3$ ceramics can provide a method to improve the figure of merit. At a nanometric range, the properties in the grain can be altered when quantum phenomena, as a electrons gas, have a fundamental role in this regime[52]. However, at a micron and sub-micron range, the grain boundary structure is one important parameter that controls the TE properties. The increase of grain boundaries will increase the phonon scattering in the polycrystalline structure, leading to a decrease of the thermal conductivity[1]. Additionally, the reduction of the grain size will increase the scattering of the phonons with shorter mean free paths (MFP) at the grain boundaries, creating a wider range of scattered phonons[1]. Although, this effect is diminished with the increasing temperature, since the MFP of the phonons is shortened at higher temperatures, reducing the possible scattering between GB and phonon. Figure 13 represents this

reduction from bulk single crystal to 50nm polycrystalline ceramics. In this case, the lowest thermal conductivity coefficient (3,4 $Wm^{-1}K^{-1}$) is reached at 1000 K for a grain size with 50 nm, 20% less than the single crystal bulk[1].

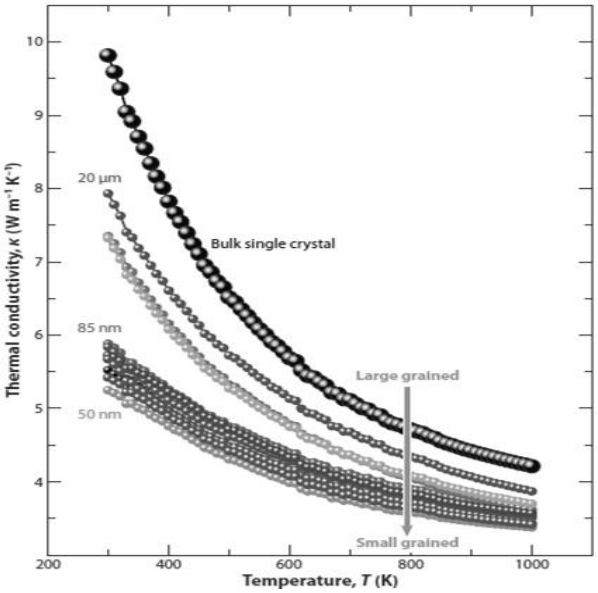

Figure 13 – Thermal conductivity dependence with temperature and grain size [1]

The decreasing dependence of *k* with the temperature is attributed to the lattice component of the thermal conductivity that due to the reduction of the phonons free mean path spectrum, decreases with the temperature[33].

The reduction of grain size can additionally present drastic improvements in the Seebeck coefficient of the material. A study presents Seebeck coefficient results in three different STO undoped materials: a single crystal, micro-size grains and nano-size grains[53]. In this undoped case, the sample with smaller grains shows a higher Seebeck coefficient (Figure 14), which is explained, according to the authors, by the increasing of grain boundaries' volume fraction in the material[53].

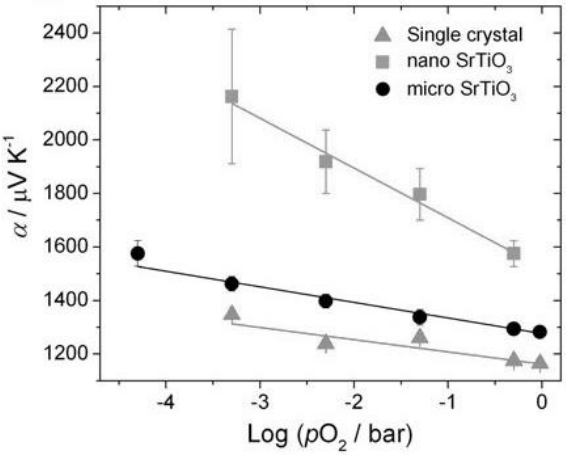

Figure 14 - Seebeck coefficient dependence on the oxygen pressure for different grain size undoped STO[53]

The electrical conductivity of undoped $SrTiO_3$ has different dependence on the grain size variation, depending on the existent charge carrier's. Due to the insulator behaviour of undoped STO, only in a high oxygen pressure conditions, the electrical conductivity by holes occurs[54]. The variation of the grain size produces higher conductivity in bulk material than in nanocrystalline ceramic, which is the opposite case of conduction originated by electrons[54]. At a lower oxygen pressure, the concentration of electrons in the material increases, creating an n-type material that is more conductive in a material with smaller grain size than in bulk materials, visible in the Figure 15. This may be seen as an evidence for the possible behaviour in the electrical conduction for a B site doped $SrTiO_3$. However, other considerations as migration of the dopant to the GB or blocking effects of the GB to the electron transport can reduce the electric conduction of the nanocrystalline material.

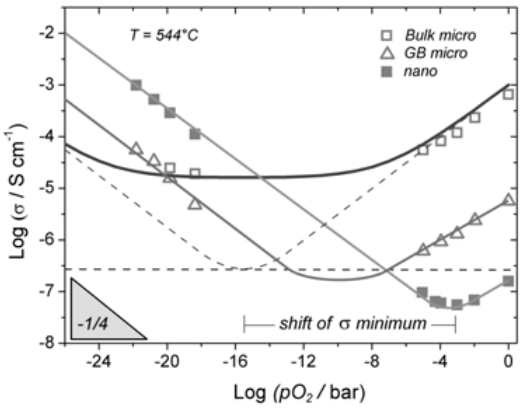

Figure 15 -Variation of electrons and holes conduction with oxygen pressure for different grain size STO[54]

Additionally, the dependence of σ with the temperature is mainly connected to the charges mobility, as the concentration of electrons is constant. The charge carriers are only dependent on the amount of dopant and reducing atmosphere, since the concentration values are fairly higher when compared with intrinsic mechanisms for the production of electrons-holes pairs. This behaviour defined the Nb doped $SrTiO_3$ as a degenerate semiconductor, that has the decreasing mobility attributed to the increasing of the phonon scattering, similar to a metal[33].

Other possible solution for the improvement of the thermoelectric properties is the embedment of the polycrystalline material in a glass matrix, creating a glass-ceramic composite. This approach has as the principal goal the reduction of the thermal conduction due to the presence of the glassy phase to increase the phonon scattering and at the same time, maintain the other thermoelectric properties. Improvements in *k* and S were observed in this system, nevertheless, the reduction in the electrical conductivity is extreme, obtaining ZT values around 0.001[55].

2.3.3 Sintering of Strontium Titanate

The consolidation of inorganic powder compacts using thermal energy in order to fabricate ceramics is defined as sintering process[56]. The solid state sintering is characterized by the densification of the compacted powders in solid state at a sintering temperature[56]. In this case, there is no formation of liquid phases, since the temperatures used are below the melting temperature of the powders. In the solid state sintering, three different stages usually divide the process. In the initial stage, the shape of the grains is changed with the formation of necks between the particles, resulting in the creation of pores between the grains. This first stage is characterized by a limited compact linear shrinkage that generally varies from 2% to 3%. The second stage is referred as intermediate state where the majority of the densification occurs, up to 95%. The elimination of open pores arises in this part of the process, while the grain boundaries are being formed. In the final stage, the densification of the closed and isolated pores contributes for the final densification of the ceramic[56]. The condition before the sintering process and the three stages described are visible in the Figure 16.

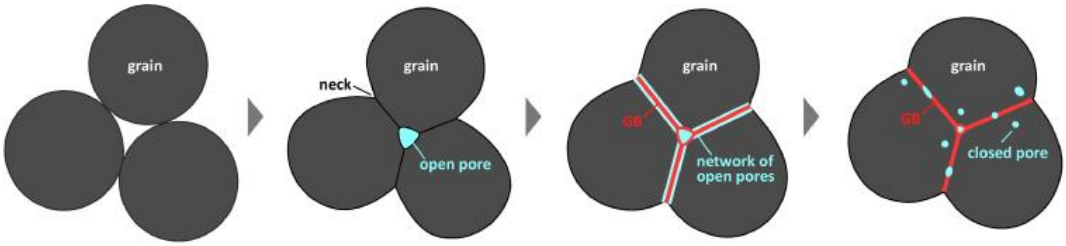

Figure 16 – Stages of the Solid state sintering process[57]

The decrease in the surface free energy of powdered compacts is the driving force for sintering process. First the modification of the solid-vapour to solid-solid interfaces lowers the free energy of the system, via the densification. Additionally, the coarsening of grains enables the reduction of free surface energy and specific grain boundary by the formation of larger grains[56].

The growth of the grains can be separated in two different types: normal and abnormal, presenting single and bimodal distributions, respectively. The first one is characterized by a constant and simple growth of the grain with the sintering time, while the abnormal grain growth presents a bimodal grain size distribution, with the formation of a fine grains matrix with some large grains[56].

In the processing of $SrTiO_3$, both types are reported in the literature[47]. The mobility of the grain boundary is the main factor for the differences in the growth of the grains. The mobility varies widely in different materials but also with some other parameters as sintering temperature, pressure, atmosphere, dopants and initial grain size distribution[47]. The presence of dopants and the use of reductive atmosphere, which are parameters fundamental to produce TE $SrTiO_3$, can affect material densification and grain growth. The formation of ionic vacancies alters the grain boundary mobility, with the possibility of segregation of the dopant in the grain boundary[58].

Some studies report that the variation on the Nb concentration and sintering temperature produces differences in the microstructure and density of the samples[59]. The dependence of the relative density with the concentration of Nb is reported to be inversely proportional, for values below 2,2% of Nb. The grain size variation is more complex, since the temperature also has an important role in the growth mechanism. It is reported the minor increase of the grain size for concentrations up to 2,2% (5 to 15 μm), with the sintering temperature below the eutectic temperature (1420ºC). For higher temperatures,

the samples present larger grains (90 μm), nevertheless the dependence with the Nb concentration is more complex; a maximum peak for the grain size is observed at 0,8% of Nb, decreasing abruptly until the higher concentration studied (2,2%)[47]. The micrographs of 1,2% Nb doped sintered samples with two different temperatures are visible in Figure 17.

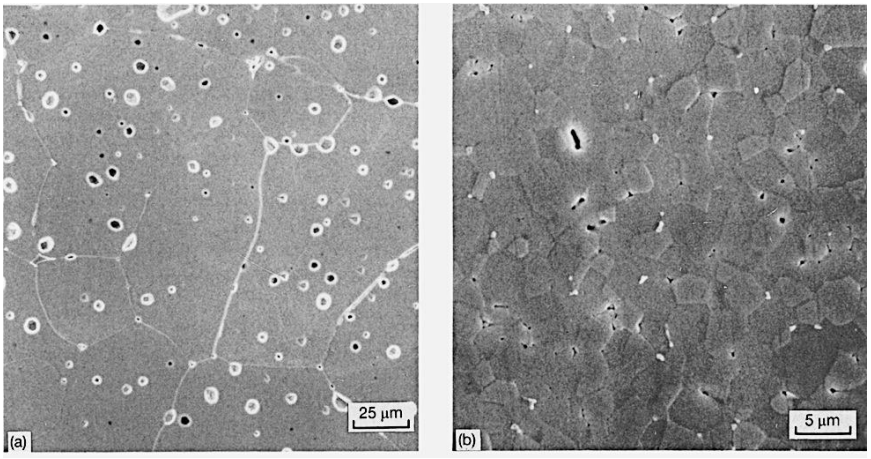

Figure 17- SEM micrographs of 1,2%Nb doped STO for a) 1480ºC for 4 hours and b) 1420ºC for 8 hours in air.[47]

The effect for higher Nb concentrations it is still unreported. Additionally, it has been reported an higher segregation of the Nb ions in the grain boundary when a H_2 atmosphere is used, instead for a air atmosphere[60]. The images of the different sintering atmospheres are visible in Figure 18. It is visible the presence of larger grains in the sample sintered in air, when compared with the one sintered in H_2.

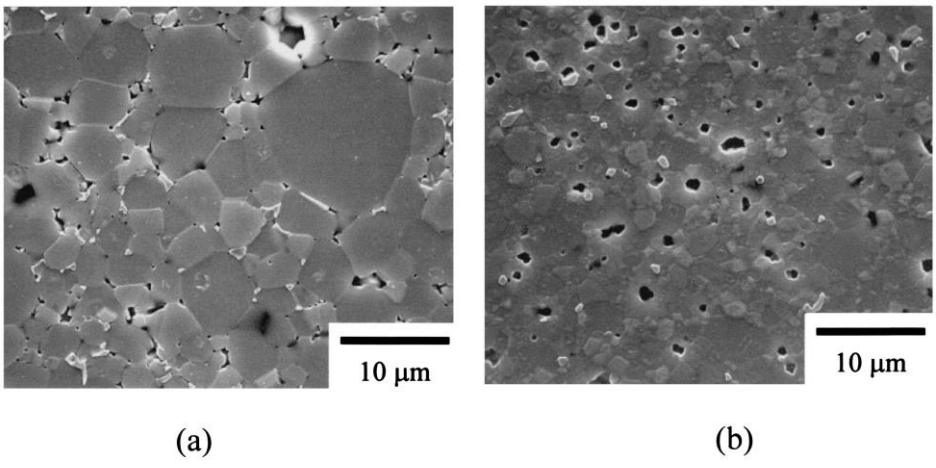

Figure 18 - SEM of 2,4% Nb doped STO sintered for 2 hours at 1460ºC a) in air and b) in H_2[60]

CHAPTER 3

Experimental Procedure

3. Experimental Procedure

The samples production was divided in four main parts: powders preparation, reduction of particle size, sintering and annealing processes. These four steps allow the production of different pellets with distinct densities and grain size distribution. The preliminary samples were undoped pellets of both materials ($SrTiO_3$ and RP1), used to establish the milling processes, followed by the preparation of dopant samples. The amount of dopant used was 5% and 20% for $SrTiO_3$ ($SrTi_{0,95}Nb_{0,05}O_3$ and $SrTi_{0,8}Nb_{0,3}O_3$ respectively) and 5% for RP1 samples ($Sr_2Ti_{0,95}Nb_{0,05}O_4$). The values used reflect the maximum amount of dopant used that produces single-phase ceramics.

3.1 Preparation of the powder

The samples were prepared by a solid-state reaction of mix powders with the accurate stoichiometry of TiO_2, $SrCO_3$ and Nb_2O_5. The powders were mixed by ball milling for 5 h, with zirconia balls in an ethanol medium. The calcination was performed for 2 hours at 1200 ºC with an increasing and decreasing rate of 10 degrees per minute.

3.2 Reduction of the particle size

The powders were again ball milled in Teflon jars with ethanol in with a proportion of zirconia balls of 1:10 the mass of the powder, with a velocity of 300 rpm. The study of ball milling variation with time was performed, reaching the optimal value of 72 hours. The double distributions of grains detected after the milling process required a centrifugation stage to separate the powder. The sample was dissolved in water, with a concentration of 20g/L, mixed in the ultrasounds for 5 minutes and centrifuged for 1 min with a rotation of 1000 rpm. The slurry and the precipitate were collected, filtered and dried in order to obtain the separated powders.

3.3 Ceramics preparation

Two different types of pellets were prepared. Circular pellets of 10 mm in diameter and rectangular pellets of 15x5 mm were prepared by uniaxial pressing at 20 KPa for 30 sec, followed by cold isostatic pressing at 200 MPa for 15 min.

Different groups of samples were produced in order to obtain distinct samples, with different characteristics. In the first trial the $SrTiO_3$ samples (5% and 20% doped) were sintered at 1450 ºC for 5, 10 and 20 hours with an increasing and decreasing rate of 10 degrees per minute in a air atmosphere. The samples were additionally reduced by a thermal annealing at 1400 ºC for 60 hours in a H_2/N_2 atmosphere. The temperature used for the annealing stage is below the eutectic temperature (1420ºC).

The second group of samples had the sintering time fixed (10 hours) and a variation on the annealing time. The $SrTiO_3$ samples (5% and 20% doped) were sintered at 1450 ºC for 10 hours with an increasing and decreasing rate of 10 degrees per minute in air. The RP1 samples (5%doped) had the same heating conditions, however, an Ar atmosphere was used in this case. The samples were reduced by a thermal annealing at 1400 ºC for 1 minute, 10 and 20 hours in a H_2/N_2 atmosphere.

The final group of samples produced used the finer powders separated by centrifugation and filtration. Only the two compositions of $SrTiO_3$ were produced with a sintering time of 10 hours and an annealing of also 10 hours. All the other conditions were kept constant as before for the two thermal treatments.

3.4 Analysis techniques

3.4.1 Coulter Multisizer - Particle Size

The determination of the powders' particle size was performed using a Coulter Multisizer (LS230, Beckman Coulter, Inc., USA). The operation system of this device is based on the diffraction pattern of laser light scattered by the powders surface, called diffraction pattern[61]. The laser light beam, with a wavelength of 750 nm, passes trough the particles suspended in a liquid, producing the scattering pattern that is collected in three

sets of detectors, after passing trough Fourier optics lenses[61]. These optical lenses are responsible for the focusing of each particle pattern as seen in the Figure 19.

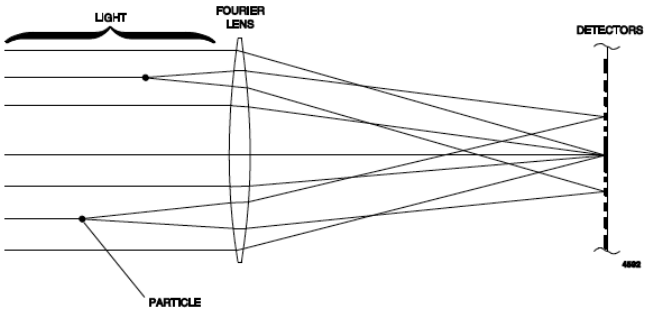

Figure 19 - Fourier Lens Focusing[61]

The detector that measures the flux in every instant follows the diffraction pattern of each particle, creating a composite image of the whole sample. The average flux of each pattern is the quantity used to correlate with the area of the particle, providing the radius of each particle. The size of the particle is always approximated to a sphere, since the method does not distinguish between different shape powders. The range of sizes detected by this method is limited from 0,4 μm to 200 μm, however, the same equipment have another mode that can allow the determination of smaller particles. The Polarization Intensity Differential Scattering (PIDS) is used in this device to detect particles with sizes lower than 0,4 μm, reaching until 0,04 μm. This method uses sequential images produced by beams with different wavelengths and polarization, to produce the diffraction pattern that is used to determine the particle length, improving the sensibility of the equipment[61]. The trial is preformed in suspension with a concentration of 0,5 g/L, previously ultrasonicated (Branson, USA) for 5 minutes.

3.4.2 X-Ray diffraction

The analysis of the crystallographic structure of the powders and samples was performed by X-ray diffraction (XRD). The interaction of the X-rays with the atoms of the crystal allows a suitable probing of the atoms positions and consequentially their arrangement in the crystal structure. This interference of deflected X-rays is possible due to the small wavelength of these electromagnetic waves, comparable to the lengths between crystallographic planes, producing diffraction patterns that can be subsequently detected[62].

The variation of the incident beam in the sample will satisfy different diffraction conditions determined by the Bragg's equation:

$$2dsin(\theta) = n\lambda$$

where d corresponds to the distance between crystallographic planes, θ is the diffraction angle of the light, n is the order of diffraction and λ is the wavelength used that the Cu K, equals to 0,1519 nm. The detection of the XRD peaks can be then related to the lattice parameter and structure of the crystalline material[62], enabling the detection of different phases in the sample and calculation of the theoretical density of the material. The analysis was performed at room temperature using an X-Ray diffractometer (Rigaku D/Maz-B, Cu Kα). In the calcined powders, a previous gridding was preformed to avoid agglomerations and improve the homogeneity of the samples. In the pellets, the analysis was generally carried with polished surfaces. The range of the spectrum obtained varied from 15º to 80º in the diffraction angle (2θ) with a scanning rate of 3 degrees per minute.

3.4.3 Density – Geometrical and Archimedes

The densities of the green body's samples were measured by the determination of the weight and geometrical volume since the immersion in liquids was impossible due to low aggregation between the powders. The ratio between the two quantities provide the density:

$$\rho_{geo} = \frac{m}{V_{geo}}$$

The determination of the density in sintered samples was measured by the Archimedes' method immersing the samples in ethylene glycol. The density was calculated bye the following equation[63]:

$$\rho_{Arc} = \frac{\rho_{liq} W_{air} - \rho_{air} W_{liq}}{V_{air} - W_{liq}}$$

where W_{air} and W_{liq}, corresponds to the weights of the pellets in air and ethilenoglicol, respectively; and ρ_{air} and ρ_{liq}, corresponds to the density of the respective mediums. The density of the air was considered as $\rho_{air} = 0{,}001185$ g/cm^3 and the density of the ethylene glycol was considered as $\rho_{liq} = 1{,}11$ g/cm^3. The theoretical density of the samples was

assumed to be 5,12 g.cm^{-3} for undoped $SrTiO_3$, 5,017 g.cm^{-3} for undoped RP1. For the doped samples, the theoretical density was calculated from the lattice parameter provided by the XRD patterns, for each composition.

3.4.4 Optical Microscope (OM)

The optical microscope (OM) was essential in this work, in order to have a general view of the specimen surface, before the SEM operation. This technique is based on the magnification of an image using optical lenses that create an amplified micrograph of the sample[64]. The OM allows a preliminary view in terms of surface roughness, grain boundary revelation and heterogeneity of the sample, providing an easy way to compare qualitatively different samples. The control of contrast, colours and brightness is fundamental to highlight the information provided by the image. The micrographs also allow the determination of the average grain size of the pellets in the case of large grains. The equipment used for this analysis was a Nikon, HFX-IIA with a maximum magnification of 200 times.

3.4.5 Scanning Electron Microscope (SEM)

The microstructure imaging of the samples was obtained using a scanning electron microscope (SEM). This technique allows the formation of images that display the topography of the sample through the interaction of electrons with the surface of the material. The SEM is grounded on the detection of secondary scattered electrons emitted by the atoms that were previously excited by the electron beam of the microscope (primary electrons)[65]. The analysis of each point of the sample enables the creation of a scanned image with different brightness levels, reflecting the roughness differences of the specimen that are determined by the amount of electrons detected. The energy dispersive spectroscopy (EDS) was additionally preformed to analyse the chemical composition of the sample in a microscopic scale, being elemental maps created and overlapped with the SEM micrographs.

In order to resolve the grain boundary before the SEM analysis, the samples were polished and thermally etched 50ºC bellow the sintering temperature, in a H_2/N_2 atmosphere for 1 minute. The devices used to preform this technique were a Hitachi S-4000 SEM/EDS and Hitachi HR-SEM-SE/EDS: SU-70.

3.4.6 Software support: ImageJ

The use of the supporting software, ImageJ, was fundamental to analyse the SEM and OM images, in order to obtain information about the grain and grain boundary measures. Different tools presented by the ImageJ software, as the contrast and threshold control, Gaussian blur and watershed filter were used to delimit the grain boundary. Nevertheless, a visual control and manual drawing by the user were always necessary to regulate the automatic functions of the software, obtaining the more suitable delimitated pictures. The analysis of the area of the grains was performed by the automatic function of the ImageJ, which previously need the scale of the image, already provided by the image acquire equipment. The diameter determination used two possible methods: circular and Feret diameter. The first one is provided by the assumption that the grain is circular and the area obtained by the software is the area of the circle. Since this area is obtained by the equation: $A = \frac{\pi d^2}{4}$, the diameter is acquired directly from the expression. The second diameter possibility, the Feret diameter, derives from the maximum distance between two different points in the grain. This technique provides the maximum diameter value for the grain size, differing from the circular diameter that minimizes the diameter for a specific area. The Feret diameter was the option mainly used in the work.

3.4.7 ZEM-3 – Electric Conductivity and Seebeck Coefficient

The power factor properties (σ and *S*) were determined using a ZEM-3 device that allows the measurement of these properties simultaneously with variation of temperature, preformed by PhD Pablo Diaz Chao, at the group of Emmanuel Guilmeau in the CRISMAT/ENSICAEN Laboratory, University of Caen, France

The pellet in a form of a bar is positioned vertically between two blocks in a heating furnace. The sample is heated until a specific temperature, with an additional heater in the lower part to provide the required temperature gradient between the two poles. The Seebeck coefficient is directly obtained by measuring the temperatures in the lower and upper part with the thermocouples in contact with the sample, followed by the detection of the thermal electromotive force using one wire of each thermocouple[66].

The electric conductivity is determined by a 4-probe method, through the aplication of an electric current to the poles of the sample, followed by the measurement of the voltage drop between each lead, as visible in the Figure 20. This method uses one wire of each thermocouple to measure the voltage and posteriorly subtracts the electromotive force produced by the Seebeck effect[66]. Both measurements are made at the same time with a range of temperatures between room temperature and 700ºC (973,15 K).

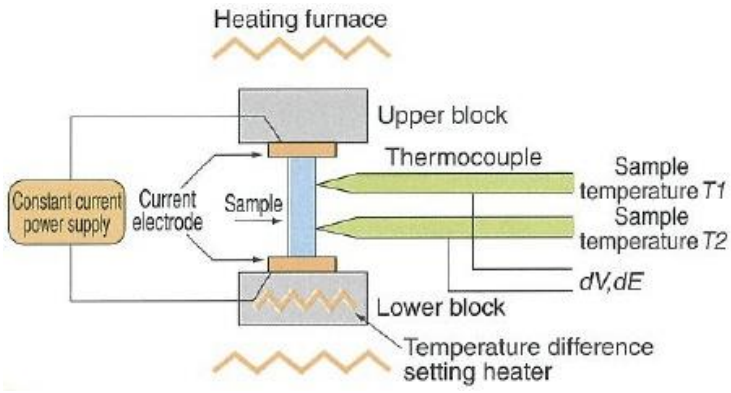

Figure 20- ZEM-3 function scheme[67]

3.4.8 Laser Flash - Thermal diffusivity

The thermal conductivity was calculated using three different properties of the materials that are related in the following equation

$$k = \alpha \rho c_p$$

where α is the thermal diffusivity, ρ is the density and $c_p$is the specific heat. The thermal diffusivity measurement is preformed through the Laser flash technique, which consists in the detection of the temperature variation with time on one side of the sample, while the other side is being heated with a laser[68]. The apparatus is usually assembled in the vertical with an alignment of the laser (heating source) on the bottom of the squared sample, and

the infrared sensor (temperature measuring device) on upper part, as visible in the Figure 21.

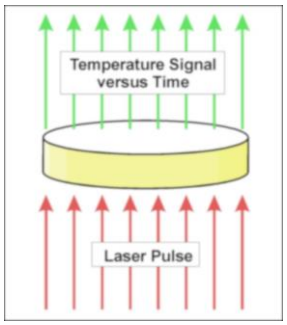

Figure 21 - Flash laser technique scheme[68]

The reduction of the energy losses is obtained trough short distances between the components and additionally the use of thin specimen (around 2mm) to prevent lateral heating. The mathematical evaluation of the temperature's time dependence enables the acquirement of the thermal diffusivity. This is the most common method to measure the thermal diffusivity due to the simple configuration, small test size, large range of diffusivity values and reproducibility. This analysis was preformed by PhD Pablo Diaz Chao, at the group of Emmanuel Guilmeau in the CRISMAT/ENSICAEN Laboratory, University of Caen, France. The samples analysed were squares with 6 mm of length and 2 mm of thickness, using a temperature range from room temperature to 700 ºC (973,15K).

3.4.9 Differential Scanning Calorimetry - Specific heat

The Differential Scanning Calorimetry (DSC) is a quantitative differential thermal analysis method that enables the determination of the specific heat. The concept behind this technique is in the measurement of the temperature differences between the reference and the sample, as function of time and temperature of the chamber[69]. This temperature difference between samples is directly related to the heat flux change. The relation between the specific heat and the heat flux can be determined by the following expression:

$$c_p = \frac{1}{m}\frac{\dot{Q}}{\beta}$$

where m is the mass of the sample, $\dot{Q}$ is the heat flux and β is the temperature-heating rate. The apparatus of the technique consists in a sample and a reference holder, with a heating block under a nitrogen flow. The chamber is heated at a temperature rate of 10 K/min and the heat flow is measured from room temperature to 500 ºC (773,15K).

CHAPTER 4

Results

4. Results

The results collected from the different analysis techniques are presented in this section. The first part is focused on the precursor powders, regarding the particle size and structure analysis. The second part focuses on the grain size and structure of the sintered pellets. Lastly, the third part of this chapter presents the thermoelectric response of the sintered samples.

4.1 Powders

4.1.1 Particle size distribution

A preliminary milling study was performed for 144 hours to analyse the particle size reduction of the powders with the time. The powders used were undoped $SrTiO_3$ and RP1 and the different average grain size are presented in Figure 22a). The distribution of the particles regarding the size are observed in the Figure 22b) for the unmilled powder (0 hours) and the final powders (144 hours).

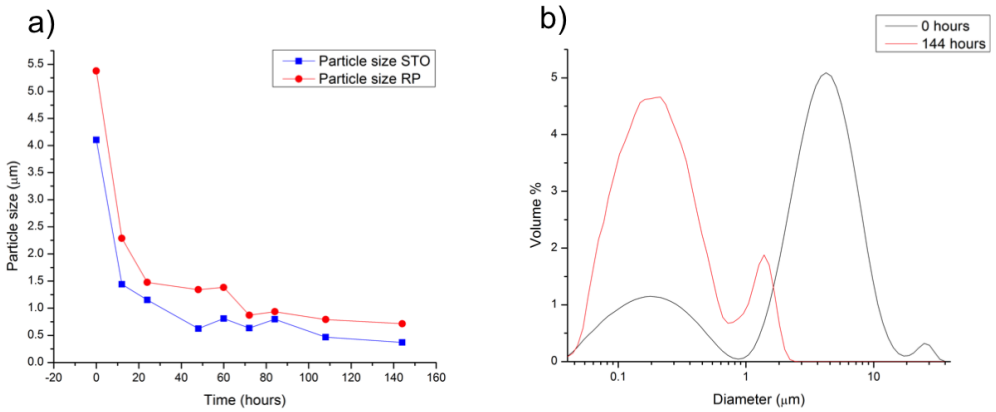

Figure 22- a) Average grain size with the variation of the milling time. b) Bimodal distribution at the beginning of the trial (0 hours) and at the end (144 hours) of the $SrTiO_3$ powder

The reduction of the average particle size is observed with the increasing of the milling time for the two compositions. A stabilization of the average particle size is observed after the 48 hours; however, the minimum time used in the milled processes for

doped samples was 72 hours. Additionally, a modification on the particle size distributions is visible (Figure 22b). In the $SrTiO_3$ powders, the intensity of the distribution's first peak (200nm) increases, while the reduction and shift of the second peak occurs, changing from 5 to 1,5 µm. The separation of the bimodal distribution of the RP powders by centrifugation and filtering is visible in the Figure 23.

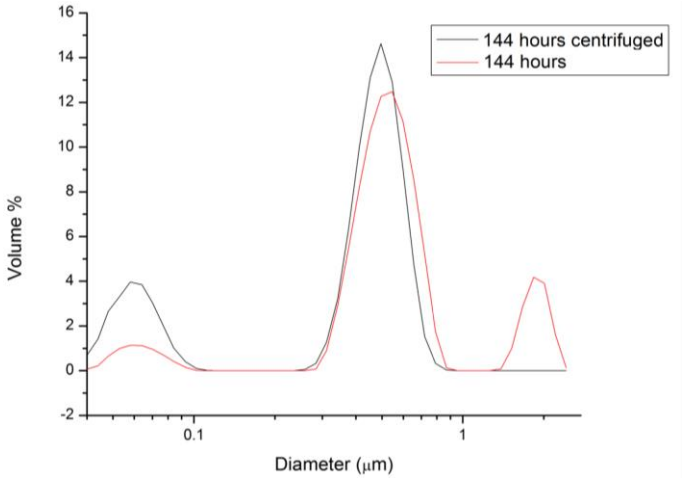

Figure 23 - Bimodal distribution of the original and centrifuged RP1 powder

The elimination of the micron-size powders is total while the concentration of submicron and nano-sized powders increased. The separation of these two sub-micron distributions was not possible to achieve. The use of doped powders had similar dependence with time and separation processes; nevertheless, the average particle size was lower when compared with undoped powders with the same characteristics.

The values of the average particle size and respective standard deviation for the doped powders are presented in the Table 1.

Table 1 - Particle size of the precursor powders

Composition	**Average (µm)**
STO 5% Nb doped – coarse particles	0,76 ± 0,7
STO 20% Nb doped – coarse particles	0,80 ± 2
RP 5% Nb doped – coarse particles	0,82 ± 1
STO 5% Nb doped – fine particles	0,32 ± 0,1
STO 20% Nb doped – fine particles	0,27±0,4
RP 5% Nb doped – fine particles	0,55 ± 0,5

4.2 Structure

The XRD spectra of the $SrTiO_3$ and the RP1 powders are visible in Figure 24. The RP case shows the presence of the RP1 phase and additional phases as RP2 ($Sr_3Ti_2O_7$) and strontium hydroxide ($Sr(OH)_2H_2O$). In the $SrTiO_3$ cases the cubic perovskite structure is obtained in both compositions with the presence of a niobium secondary phase ($Sr_4Nb_5O_{15}$) in the 20% doped pellet.

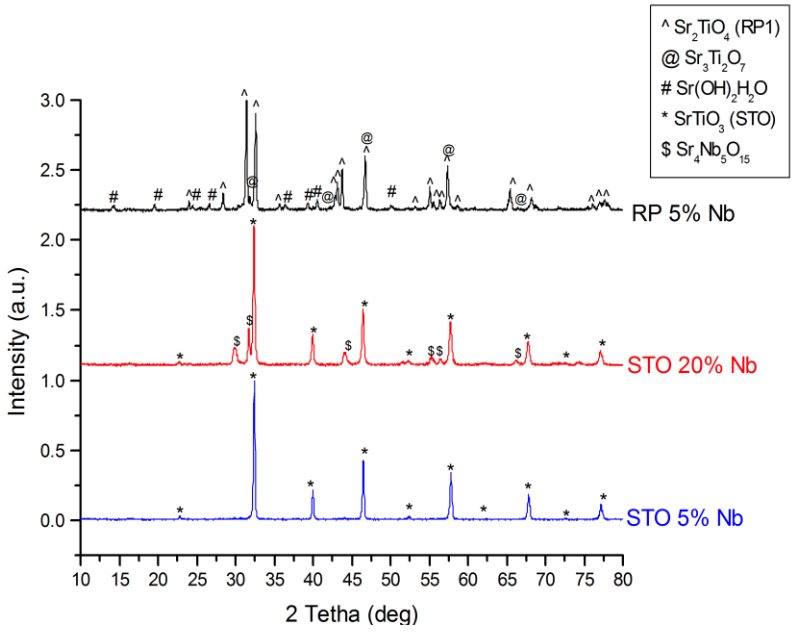

Figure 24 - XRD spectra of the calcined powders for all the compositions at 1200ºC for 2 hours

The XRD spectra of the sintered samples for 10 hours, after the annealing treatment for the same time, are visible in the Figure 25. The three pellets show a monophasic composition.

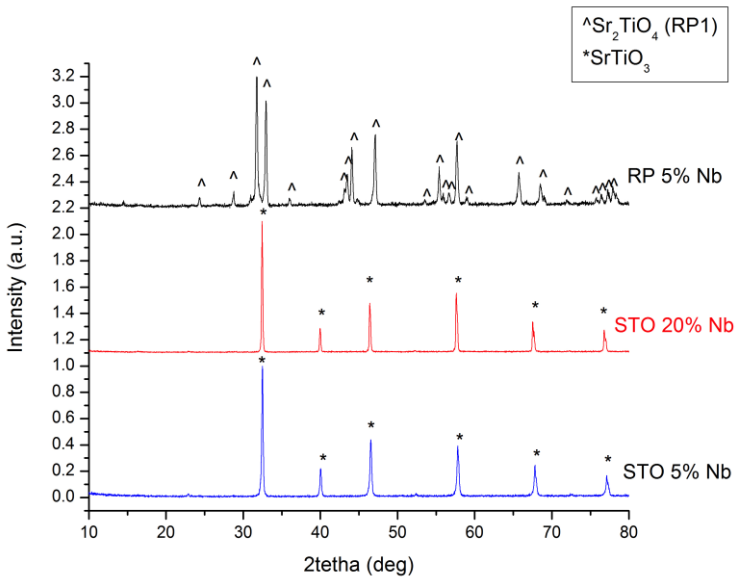

Figure 25 - XRD Spectra of sintered pellets

It is important to report that in the $SrTiO_3$ pellets the presence of secondary phases was not visible in any XRD preformed, contrarily to the RP1 case, where some samples presented secondary phases of $Sr_3Ti_2O_7$ (RP2) and $SrTiO_3$.

4.3 Density

The analysis of the XRD spectra additionally allowed the identification of the peaks' shifts from the original position, evidencing a modification of the lattice parameters. The lattice modification combined with the differences in the molar mass due to doping implied a variation in theoretical densities. The calculation of the new parameter and consequent theoretical densities, visible in the Table 2, was based on the XRD spectra, using the XRD software JADE 9 and molar mass differences. The increase of the amount of dopant caused a widening of the lattice parameter and increasing of the theoretical density, where the rise is higher in the 20% doped case for both properties. In the 5% Nb doped the variation of lattice parameter is +0,18pm, while in the 20% Nb doped this variation is +0,55pm. The density variation for the 5% case is +0,054 $g.cm^{-3}$ and +0,227 $g.cm^{-3}$ for the 20% Nb doped sample. For the RP1 case, the variation of the a an b parameter are negative (-2,28 pm), while in the c parameter the variation is positive (+16,8pm), resulting in a variation of density of +0,031 $g.cm^{-3}$.

Table 2 - Lattice parameter modifications, comparison with undoped $SrTiO_3$ and theoretical densities calculation

Composition	a and b(nm)	Δa and Δb (pm)	c(nm)	Δc(pm)	ρ (g.cm^{-3})	$\Delta\rho$ (g.cm^{-3})
STO 5% Nb	0,39064	+0,18	0,39064	+0,18	5,174	+0,054
STO 20% Nb	0,39101	+0,55	0,39101	+0,55	5,347	+0,227
RP 5% Nb	0,38612	-2,28	1,2768	+16,8	5,048	+0,031

The green body densities of the pellets were determined by geometrical calculation, being the obtained values around 60% for the majority of the samples. The densities of all analysed samples are indicated in Table 3. The variation of the relative density of the pellets is visible in Figure 26 for sintering time variation and in Figure 27 for varied annealing time.

Table 3 - Densities and relative densities of all samples

Composition	Sintering conditions (h)	Annealing conditions (h)	Density (g.cm^{-3})	Relative Density (%)
STO 5%Nb	5	60	4,4306	93,0%
	10	60	4,7171	94,4%
	20	60	4,9909	97,8%
	10	0,0167	4,3926	84,9%
	10	10	4,8653	94,0%
	10	20	4,7719	92,2%
	10 (finer powders)	10	4,9142	95,0%
STO 20%Nb	5	60	4,8637	91,0%
	10	60	5,0582	97,0%
	10	10	5,1332	96,0%
	10	20	5,2299	97,8%
	10 (finer powders)	10	5,1718	96,7%
RP 5%	10	0,0167	4,6881	93,4%
	10	10	4,7132	94,4%
	10	20	4,074	89,5%

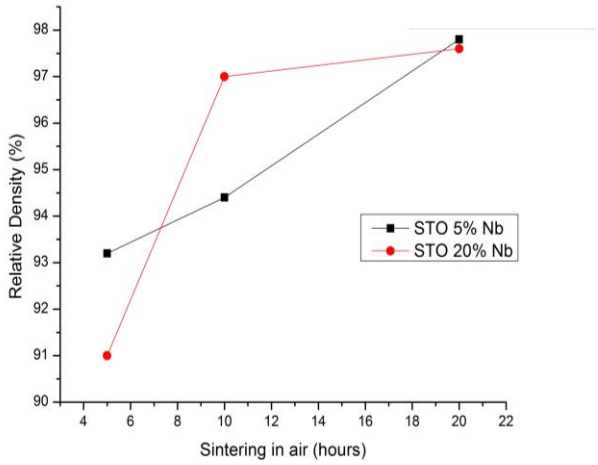

Figure 26 - Variation of relative density with the sintering time for $SrTiO_3$ pellets for both compositions and annealed for 60 hours

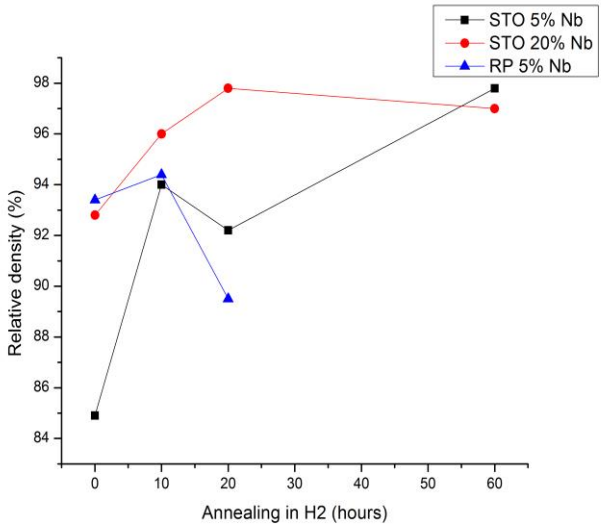

Figure 27- Variation of relative density with the annealing time for $SrTiO_3$ and RP1 pellets for both compositions and sintered for 10 hours

In both thermal treatments is visible a tendency for higher densification with the increasing of the process time, with a few exceptions. The densities are a higher than 90%, except in the $SrTiO_3$ 5% doped case, where the annealing stage was preformed for 1 minute, presenting density values of 84,9%. In the samples sintered and annealed for longer times, the densification is higher than 95% in the majority of the samples. RP1 shows a variation of density different from the $SrTiO_3$ cases. In this samples, a decrease of density is visible for the longer annealing times, 20 hours. Lastly, the densities of the samples prepared with finer powders are higher than of the samples prepared with coarser

powders under the same thermal treatments. In the 5% doped case, the density is 95%, while in the 20% doped case the density is 96,7%.

4.4 Grain size

The micrographs of the 5% Nb doped pellets, sintered for 10 and 20 hours and annealed for 60 hours are presented in Figure 28. The grain morphology is observed in both images, enabling the grain size analysis, with 2,1 µm and 2,9 µm of average dimensions, for the 10 and the 20 hours sintered pellets, respectively. As the annealing treatment in N_2/H_2 was the same in both samples, the grain size differences are related to the sintering stage. These samples with the lower dopant concentration present a grain growth proportional to the sintering period (Figure 28). The variation of the grain size with the sintering time is visible in the Figure 32

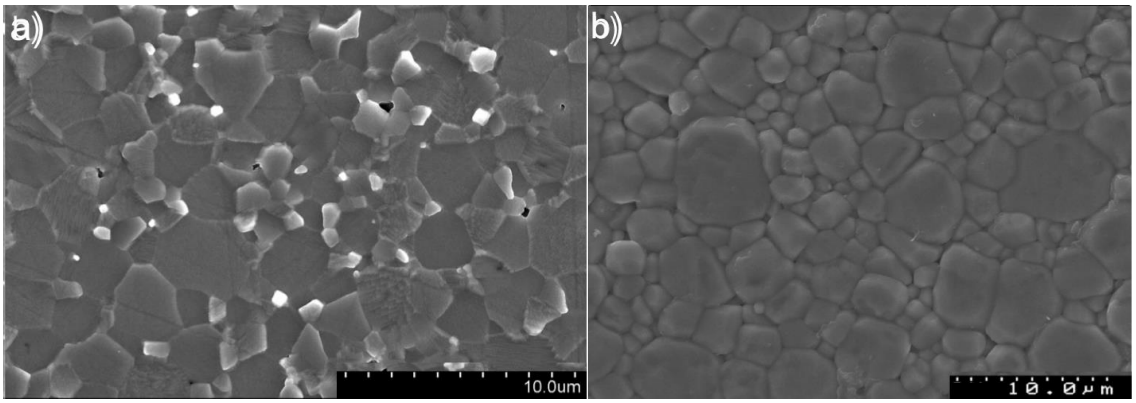

Figure 28 -SEM micrographs of STO 5% Nb doped pellets annealed in H_2/N_2 for 60 hours: a) 10 hours: G.S.- 2,1 µm; b) 20 hours: G.S.- 2,9 µm

For the 20%Nb doped samples, the effects of the sintering time variation on the microstructure are visible in Figure 29-Figure 30, which were sintered for 5, 10 and 20 hours and annealed for 60 hours, for the higher dopant concentration. The images show SEM and OM micrographs where the grains are revealed, enabling the measurement of the size. The average dimension of the grains is 22,7µm, 25,2µm and 19,5µm for the 5, 10 and 20 hours of sintering time, respectively. In these images there is no evidence of the sintering period influence on the grain size, since after the annealing treatment for 60 hours, the grains have similar sizes in the different samples. In the three samples, average

grain size around 20µm is extremely high when compared to the values after the sintering process (1 µm). Regions with finer grains surrounded by larger grains are seen in the optical microscope images (Figure 29-Figure 31).

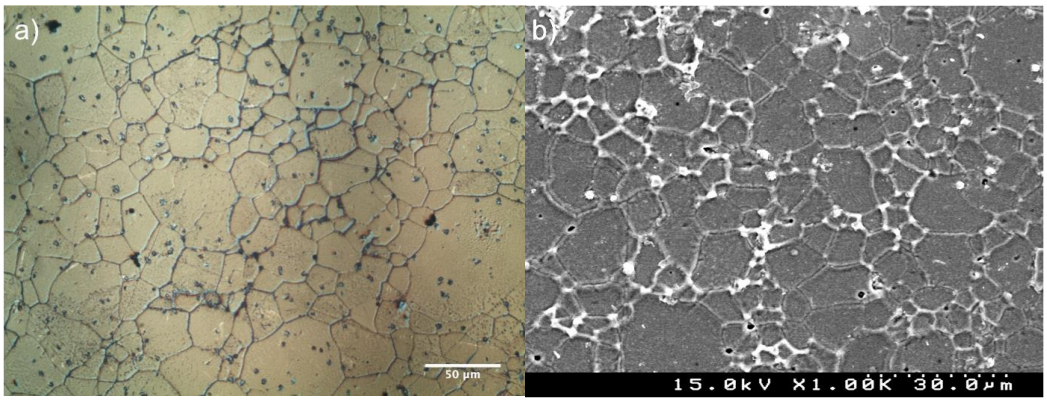

Figure 29 - a) OM and b) SEM micrographs of STO 20% Nb doped pellet – Sintered for 5 hours in air – Annealed for 60 hours in H_2/N_2 – G.S.- 22,7µm

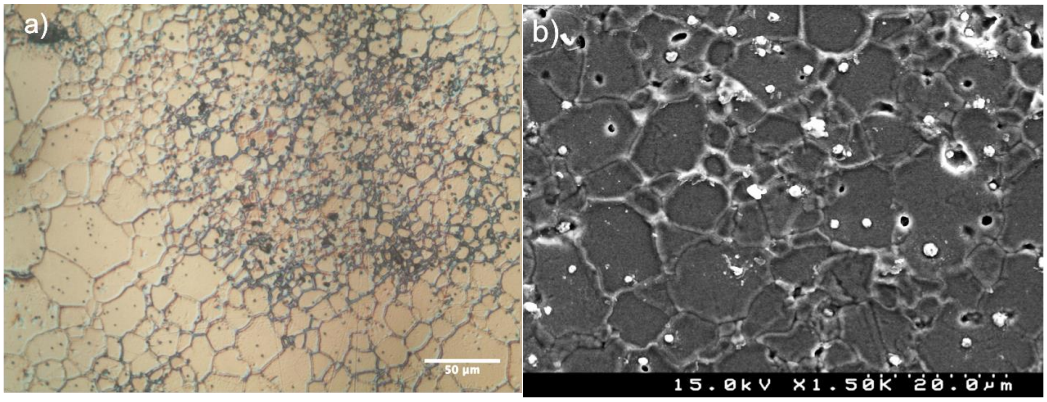

Figure 30 - a) OM and b) SEM micrographs of STO 20% Nb doped pellet – Sintered for 10 hours in air – Annealed for 60 hours in H_2/N_2 – G.S.: 25,2µm

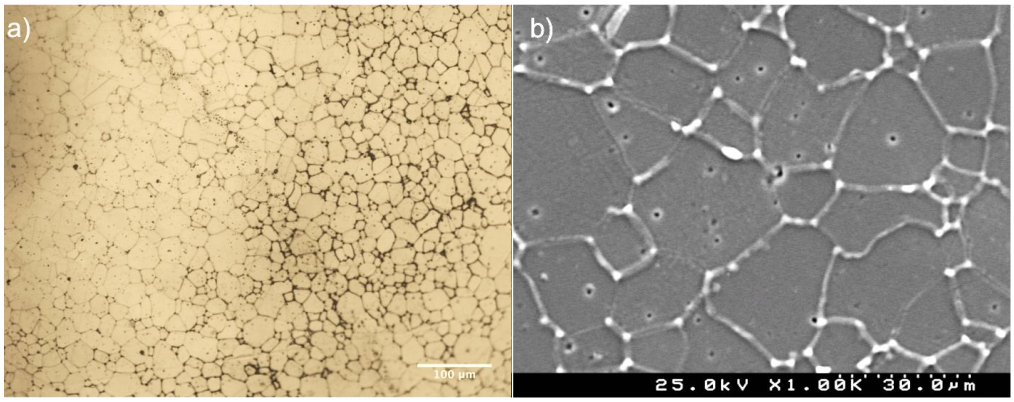

Figure 31 - a) OM and b) SEM micrographs of STO 20% Nb doped pellet – Sintered for 20 hours in air – Annealed for 60 hours in H_2/N_2 – G.S.- 19,5µm

The variation of the grain size with the sintering time for the 2 compositions of Niobium in $SrTiO_3$ is presented in the Figure 32.

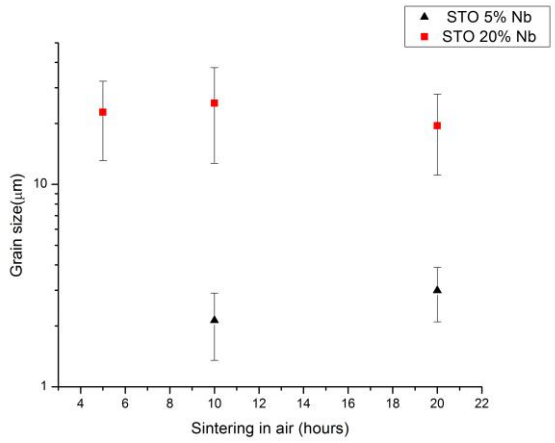

Figure 32 - Variation of Grain size with sintering time for samples annealed in H_2/N_2 for 60 hours. Both $SrTiO_3$ compositions are represented

Regarding the annealing time variation, the 5% Nb doped STO samples present a variation in morphology. In this samples, the sintering time was maintained constant for 10 hours, being visible the SEM micrographs in the Figure 33-Figure 35. As the thermal etching was not successfully executed, the showed images are from fractured sample parts. The grain sizes varied from 0,4μm in the 1 minute sample; 1,4μm in the 10 hours sample; 1,6μm in the 20 hours sample and 2,1μm in the 60 hours sample, presented before. The increase of the grains dimension with the annealing time is evident.

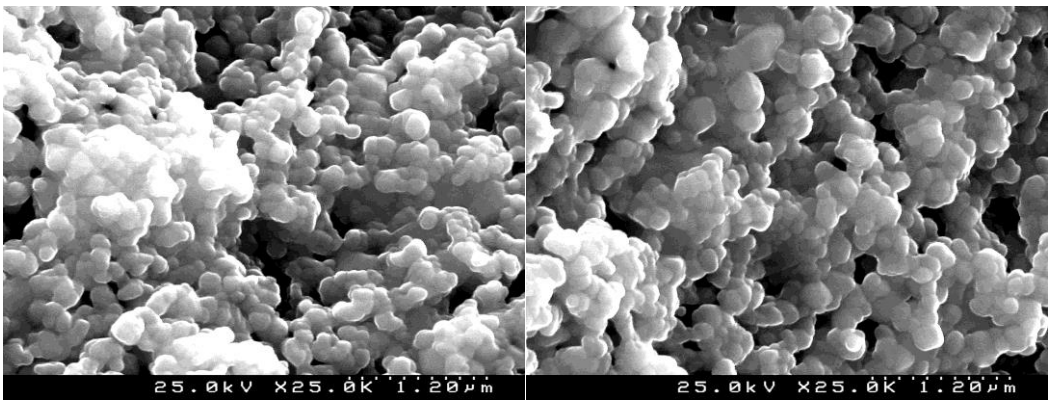

Figure 33- SEM micrographs of STO 5% Nb doped pellets sintered in air for 10 hours and annealed in $H_2/N_2$for 1 minute - G.S.-0,4μm

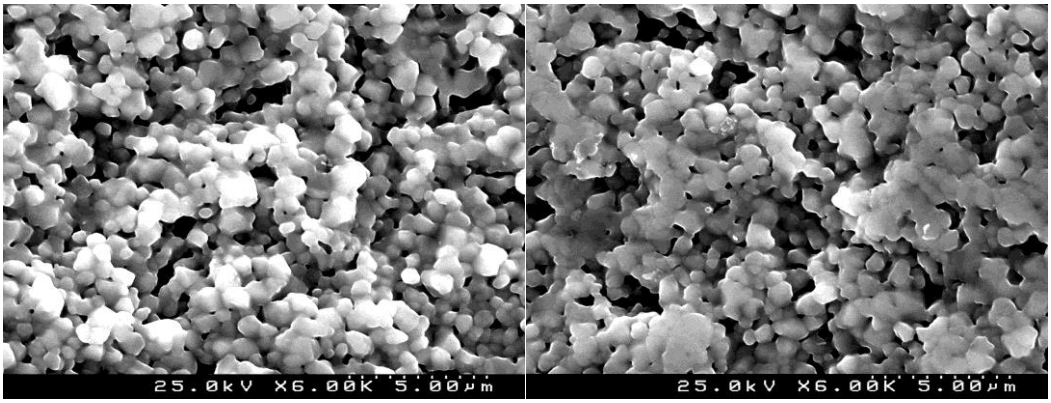

Figure 34 - SEM micrographs of STO 5% Nb doped pellets sintered in air for 10 hours and annealed in $H_2/N_2$for 10 hours - G.S.-1,4µm

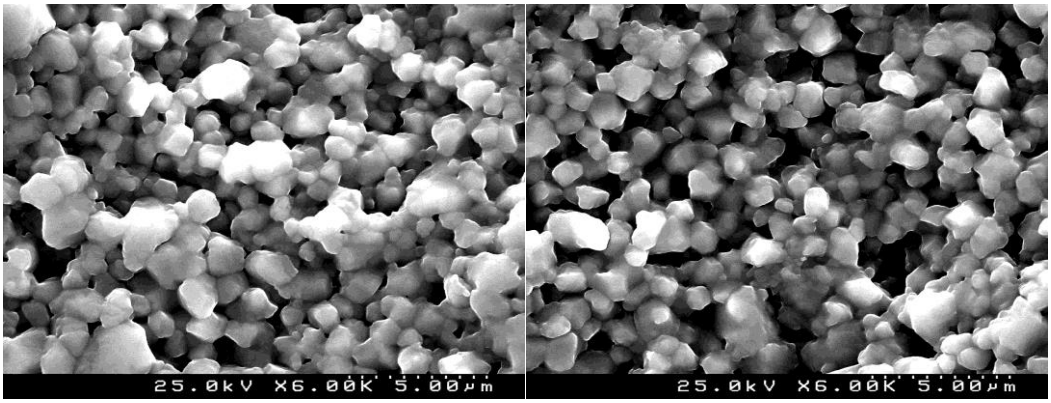

Figure 35- SEM micrographs of STO 5% Nb doped pellets sintered in air for 10 hours and annealed in $H_2/N_2$for 20 hours - G.S.-1,6µm

In the highly doped samples (20% Nb), the annealing time was varied in order to produce different average grain size between the samples, maintaining the sintering time constant for 10 hours. The micrographs of these samples are visible in the Figure 36 to Figure 38 where the grains are revelled in all the images. The grain sizes varied from 1,5 µm in the 1 minute sample; 8,0 µm in the 10 hours sample; 8,5 µm in the 20 hours sample and 25,2µm in the 60 hours sample. The increase of the grains dimension with the annealing time is evident. The morphology visible in the images shows the appearance of some regions with larger grains (20µm) in the Figure 37, contrasting with general view of the sample with smaller grains (under 10µm). The opposite situation occurs in Figure 30 where the overall morphology of the sample shows to be made of larger grains (20µm range), contrasting with some regions where the grains are bellow the 10 µm range.

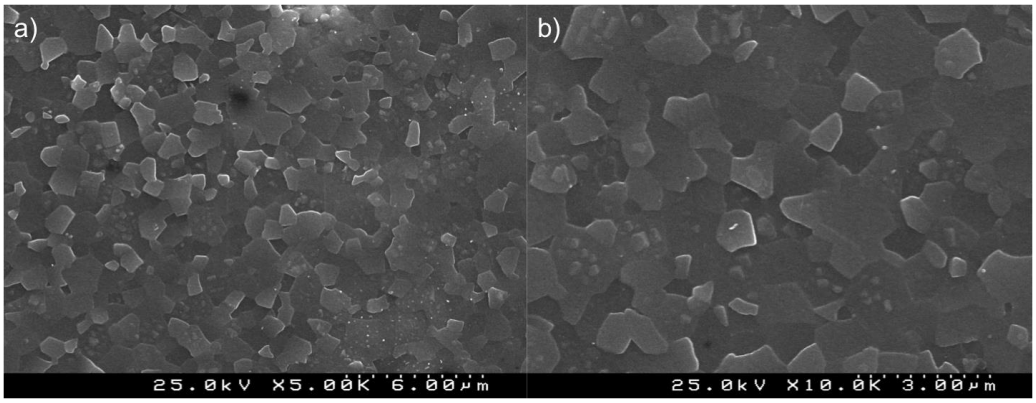

Figure 36 - SEM micrographs of STO 20% Nb doped pellet – Sintered for 10 hours in air – Annealed for 1 minute in H_2/N_2 - GS- 1,50µm

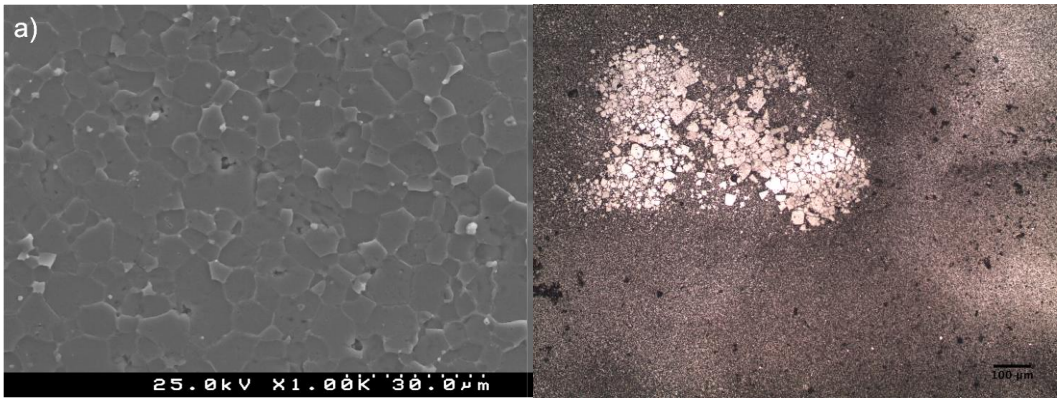

Figure 37- SEM and OM micrographs of STO 20% Nb doped pellet – Sintered for 10 hours in air – Annealed for 10 hours in H_2/N_2 – GS: 8,00µm

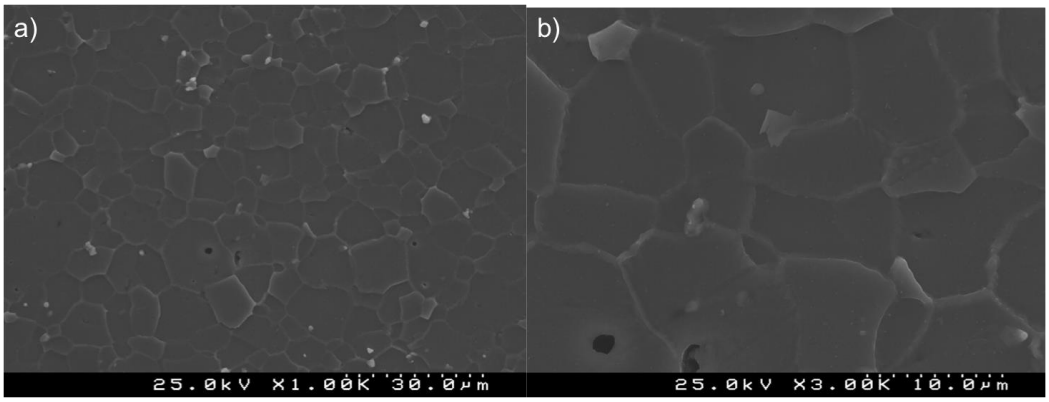

Figure 38 - SEM micrographs of STO 20% Nb doped pellet – Sintered for 10 hours in air – Annealed for 20 hours in H_2/N_2 – GS: 8,48µm

The grain size dependence with the annealing time for the Nb doped pellets is visible in the Figure 39. In the graph is observed the increase in grain size with the annealing time, while the sintering time was maintained constant.

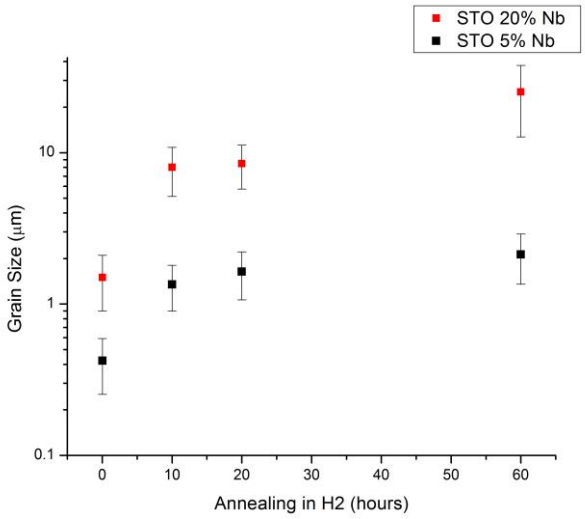

Figure 39 - Variation of Grain size with annealing time in H_2/N2 for sintered samples of 5% and 20% STO in air for 10 hours.

The micrographs of the samples prepared with fine-grained powder are presented in Figure 40 and Figure 41, for the 5% and 20% Nb doped pellets, respectively. Both samples, sintered and annealed for 10 hours, present an average grain size in the 2 µm range, with 2,25 µm for the 5% Nb doped and 2,28 µm for the 20% Nb doped. However, while in the first sample the microstructure is homogenous in all the analysed area, the second sample present a few oversized grains on the 30 µm range, with a rectangular shape (Figure 41).

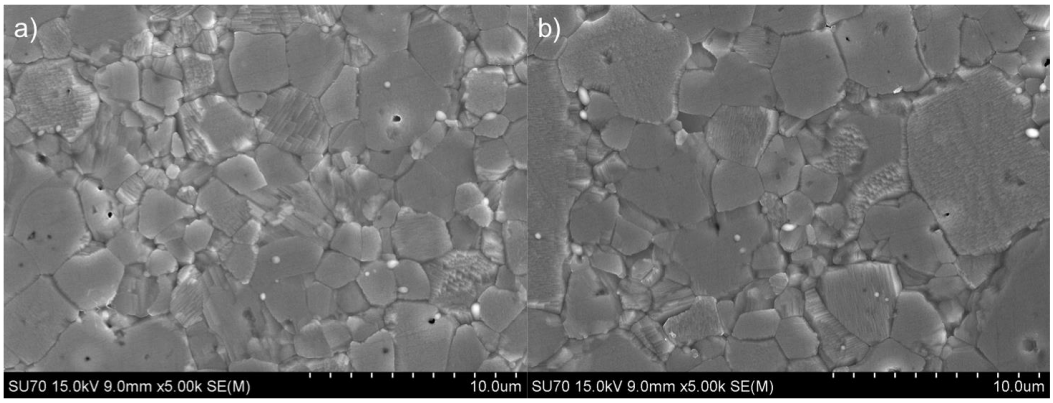

Figure 40- SEM micrographs of STO 5% Nb doped pellet with fine powders as precursor; Sintering: 10 hours in air; Annealing: 10 hours in H_2/N_2 – GS - 2,25µm

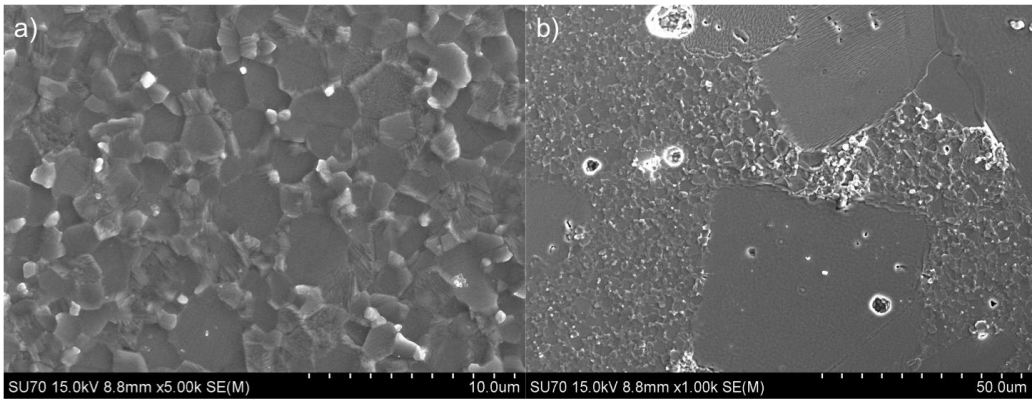

Figure 41 - SEM micrographs of STO 20% Nb doped pellet with fine powders as precursor; Sintering: 10 hours in air; Annealing: 10 hours in H_2/N_2 – GS of fine grains– 2,28µm; Larger grains - 40µm

The analysis of these larger grains was complemented with a cross section view and EDS analysis, presented in the Figure 42 and Figure 43 respectively. In the cross section images is visible the presence of these grains, confirming the existence of the morphology in the all sample. Through EDS analysis was possible to detect a higher concentration of Nb in the larger grains, 14%, while in the finer grains this amount was 11%.

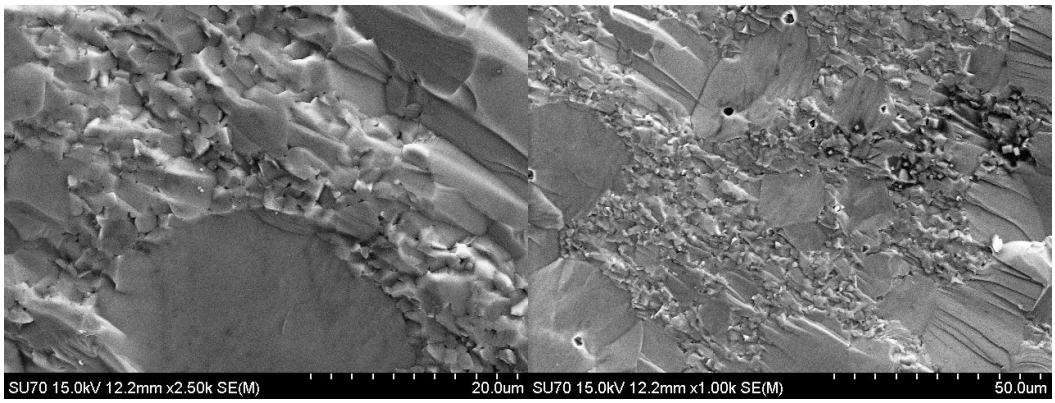

Figure 42- SEM micrographs of STO 20% Nb doped pellet with fine powders as precursor; Sintering: 10 hours in air; Annealing: 10 hours in H_2/N_2 – cross-section view.

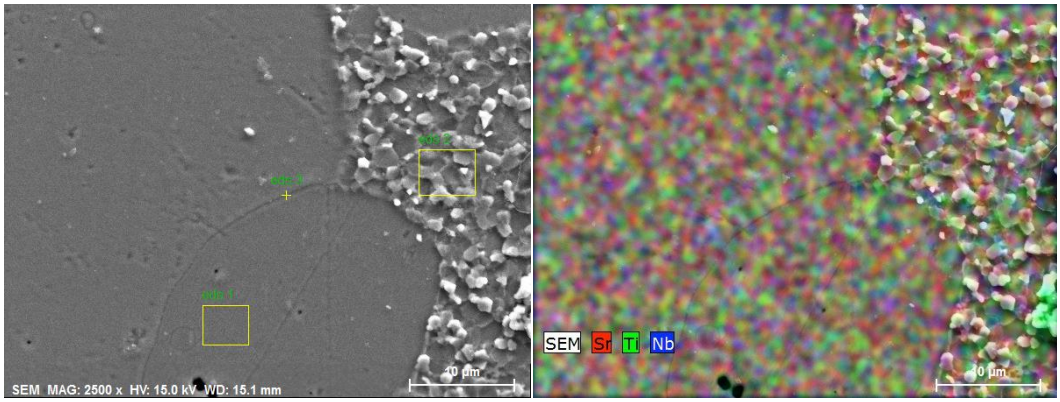

Figure 43 SEM and EDS elemental mapping (Sr, Ti and Nb) micrographs of STO 20% Nb doped pellet with fine powders as precursor; Sintering: 10 hours in air; Annealing: 10 hours in H_2/N_2

The micrographs of the RP1 samples are present in the Figure 44, for a sample sintered and annealed for 10 hours. The images show a blurred look with the distinction of some grains, however measurements of the grain size were impossible to preform, due to unsuccessful thermal etching.

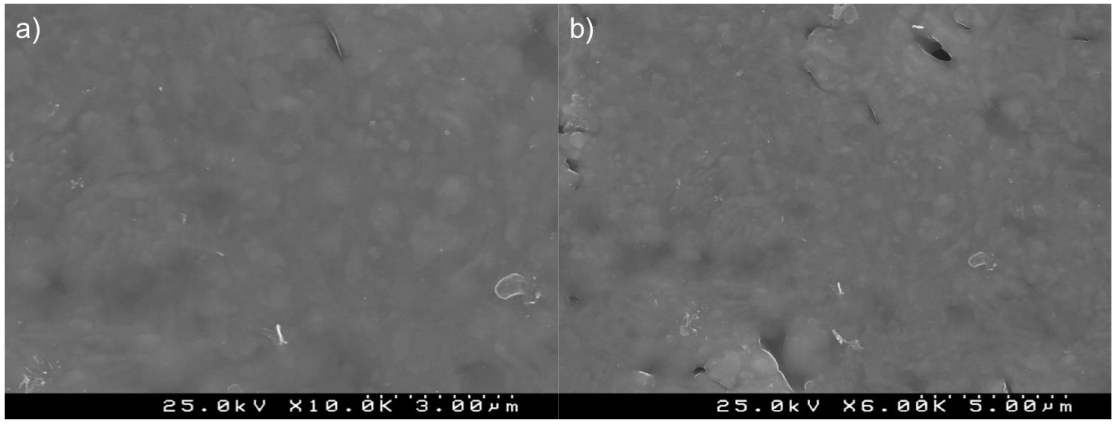

Figure 44 - SEM micrographs of RP 5% Nb doped pellet – Sintered: 10 hours in air – Annealed: 10 hours in H_2/N_2

4.5 Thermoelectric properties

The analysis of the thermoelectric properties is presented with the separation of the two $SrTiO_3$ compositions, 5% and 20%. In each composition, the sintering, annealing and precursor powders conditions are separated with the use of different colours and point shape in the graphs.

4.5.1 Electric conductivity

The electric conductivity results of the 5% Nb doped samples are visible in Figure 45. In the first set of samples, where the annealing time was maintained constant for 60 hours and sintering time was varied, the 5 hours sample shows an increasing behaviour with the temperature until the 970 K, being the only sample with this trend. The σ of this sample ranges between 2 and 27 $S.cm^{-1}$. The other samples with the annealing treatment in the 60 hours show an initial increasing with the temperature, followed by a declining, after peaking around 500 K. The final electric conductivity value is 88 $S.cm^{-1}$ for the top sample, being the one with higher sintering time, 20 hours. The variation of the annealing time shows lower conductivities values, between 0,34 and 2 at 970 K. Nevertheless, the curve shape follows the same trend, with a visible rise at lower temperatures, with a consequential decrease for higher temperatures. The sample originated from finer powders present high values of σ at 970K, where the conductivity is 55 $S.cm^{-1}$.

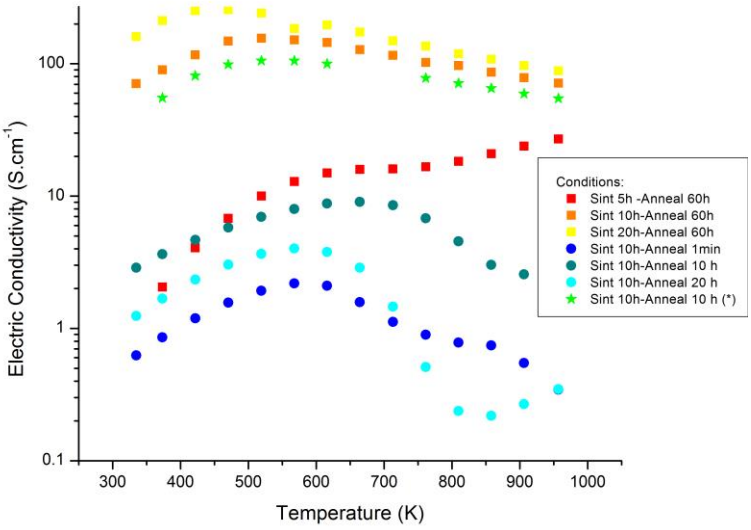

Figure 45 - Variation of the Electric Conductivity with the temperature for 5% Nb doped $SrTiO_3$. Variation of the sintering time, 5, 10 and 20 hours, for a constant annealing time, 60 hours (reddish squares). Variation of the annealing time, 1 minute, 10 and 20 hours, for a constant sintering time, 10 hours (bluish points). Sample prepared with fine-grained powders for 10 hours of sintering and annealing stage (green star)

The highly doped samples have the σ results presented in Figure 46 where a declining behaviour of σ is visible for all the samples. The samples, where the sintering time was varied, show a higher behaviour in the sample sintered for less time, varying

from 1000 S.cm^{-1} at room temperature to 268 S.cm^{-1} at 950K. In the samples with a changing annealing time, the pellet with higher conductivity is the one with a longer treatment, 20 hours. This sample shows the highest σ at room temperature, 1300 S.cm^{-1}, decreasing until the 300 S.cm^{-1} at 970K. The sample with the lowest annealing time, 10 hours, presents the lowest values of conductivity, around 200 S.cm-1 at 970 K. The last sample, with the different powders origin show a slightly different behaviour, since an initial rise of σ is visible until 500K, followed by a substantial decrease. Nevertheless, this sample shows the highest value of electric conductivity at 970K, reaching the 328 S.cm^{-1}.

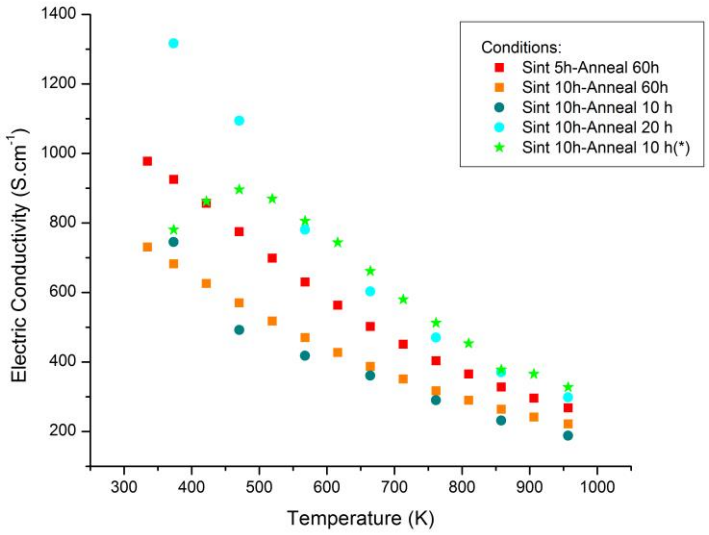

Figure 46 - Variation of the Electric conductivity with the temperature for 20% Nb doped $SrTiO_3$. Variation of the sintering time, 5 and 10 hours, for a constant annealing time, 60 hours (reddish squares). Variation of the annealing time, 10 and 20 hours, for a constant sintering time, 10 hours (bluish points). Sample prepared with fine-grained powders for 10 hours of sintering and annealing stage (green star)

The conductivity of the RP1 samples was only possible to measure at room temperature for one sample, sintered of 10 hours and annealed in H_2/N_2 for the same time. This sample show values of conductivity equal to 0,0002 S.cm^{-1}, without being possible to measure more data since it was in the limit of the measurement equipment.

4.5.2 Seebeck Coefficient

The Seebeck coefficient for the 5% doped samples is represented on Figure 47, showing a decreasing behaviour with the temperature. For the majority of the samples, the

values vary between -175 and -260 $\mu V.K^{-1}$, with a small divergence between the samples. However, the sample annealed for less time, 1 minute, shows a lower value in S, reaching -325 $\mu V.K^{-1}$ at 970 K. It is also important to stress that the sample with the different precursor powders shows the second lowest values of Seebeck coefficient, -290 $\mu V.K^{-1}$ at 970 K.

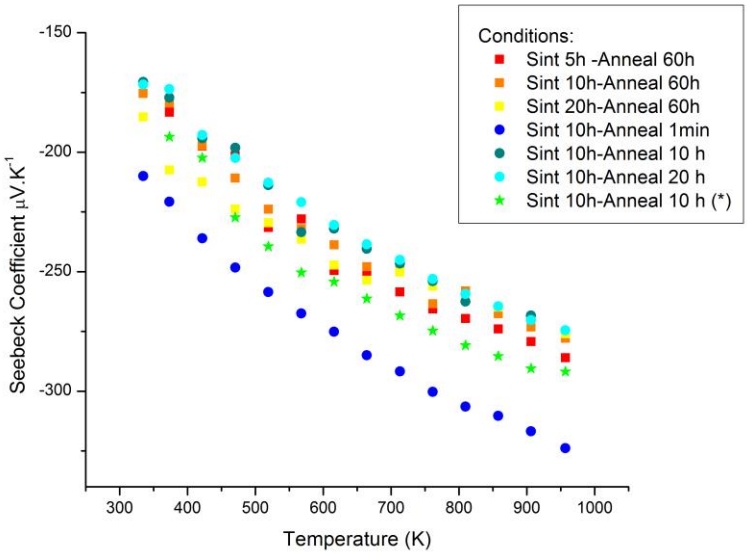

Figure 47 - Variation of the Seebeck coefficient with the temperature for 5% Nb doped $SrTiO_3$. Variation of the sintering time, 5, 10 and 20 hours, for a constant annealing time, 60 hours (reddish squares). Variation of the annealing time, 1 minute, 10 and 20 hours, for a constant sintering time, 10 hours (bluish points). Sample prepared with fine-grained powders for 10 hours of sintering and annealing stage (green star)

The plot of all the 20% Nb samples Seebeck coefficient is visible in Figure 48. The dependence with the temperature is decreasing as in the previous case, with the values of S showing to be similar in all samples, ranging between -70 $\mu V.K^{-1}$ and -150 $\mu V.K^{-1}$. Nevertheless, the sample produced with fine-grained precursor powders shows substantially lower values, reaching -178 $\mu V.K^{-1}$ at 970K

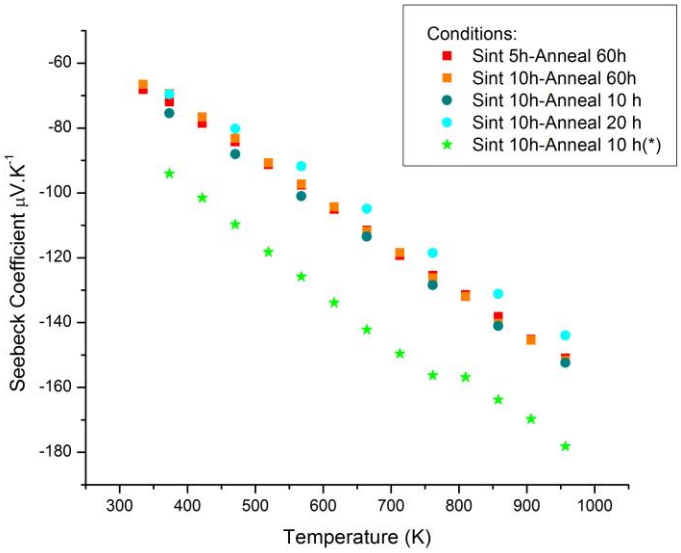

Figure 48 - Variation of the Seebeck coefficient with the temperature for 20% Nb doped $SrTiO_3$. Variation of the sintering time, 5 and 10 hours, for a constant annealing time, 60 hours (reddish squares). Variation of the annealing time, 10 and 20 hours, for a constant sintering time, 10 hours (bluish points). Sample prepared with fine-grained powders for 10 hours of sintering and annealing stage (green star)

The analysis of the Seebeck coefficient was not possible to preform in the RP1 samples, due to low conductivity values.

4.5.3 Thermal conductivity

The relation of three properties was used to obtain the thermal conductivity indirectly:

$$k = \alpha . \rho . c_p$$

where α is the thermal diffusivity, ρ is the density and c_p is the specific heat.

The specific heat was assumed constant for each composition, being previously measured by DSC. The values are present in Table 4. The values where considered constant, since there is no phase transition until the 970 K, the specific heat is reported to be stable with the temperature and the values presented are comparable with the theoretical values for the two compositions used. The value for the undoped STO material is 0,544 $J.K^{-1}.g^{-1}$.

Table 4 - Specific heat values for each composition

Composition	c_p ($J.K^{-1}g^{-1}$)
STO 5% Nb	0,474± 0,005
STO 20% Nb	0,503± 0,006

The thermal conductivity values for the 5% doped samples are presented in the Figure 49. The plot shows a decreasing dependence with the temperature, for all the cases. The dependence of the thermal conductivity with the thermal treatments is similar for both sintering and annealing processes. The longer periods of sintering and annealing processes result in an increase of *k*, in the cases analysed. Additionally, the pellet produced with the smaller particle size distribution presented similar values of the one with the same thermal conditions and coarser powders as precursors. The lowest *k* value registered is for the sample sintered and annealed for lowest time, 10 hours and 1 minute respectively, where the thermal conductivity is equal to 1,74 $W.m^{-1}.K^{-1}$ at 970 K.

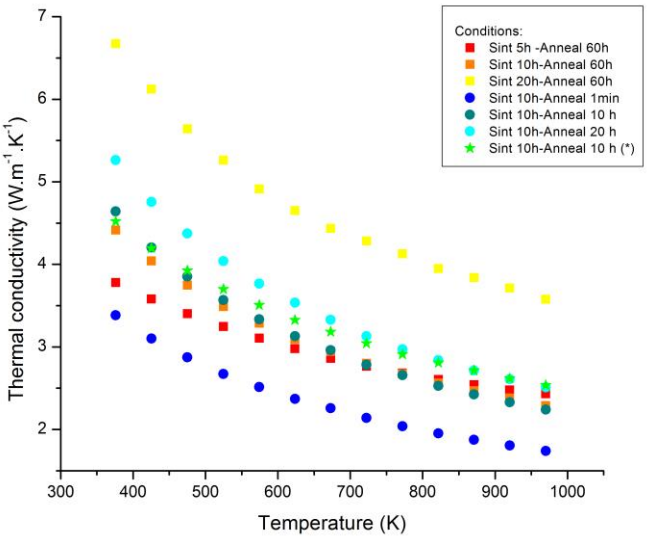

Figure 49 - Variation of the Thermal conductivity with the temperature for 5% Nb doped $SrTiO_3$. Variation of the sintering time, 5, 10 and 20 hours, for a constant annealing time, 60 hours (reddish squares). Variation of the annealing time, 1 minute, 10 and 20 hours, for a constant sintering time, 10 hours (bluish points). Sample prepared with fine-grained powders for 10 hours of sintering and annealing stage (green star)

All the 20% doped samples show a decreasing behaviour with the temperature for the thermal conductivity, visible in the Figure 50. In this case, the samples where the sintering time was varied show similar values of thermal conductivity, while the samples that were produced with different annealing times show an increasing behaviour of *k* with the duration of the thermal stage. Moreover, the pellet produced with the fine-grained powders presented, once again, comparable conductivity values to the pellet with the same thermal conditions and different precursor powders. These two samples, sintered and annealed for 10 hours, are the ones with the lowest thermal conductivity for this composition, equal to 2,4 $W.m^{-1}.K^{-1}$ at 970K.

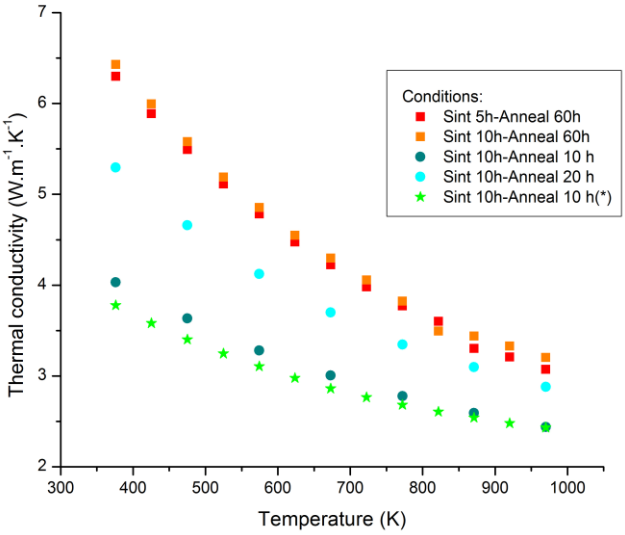

Figure 50- Variation of the Thermal conductivity with the temperature for 20% Nb doped $SrTiO_3$. Variation of the sintering time, 5 and 10 hours, for a constant annealing time, 60 hours (reddish squares). Variation of the annealing time, 10 and 20 hours, for a constant sintering time, 10 hours (bluish points). Sample prepared with fine-grained powders for 10 hours of sintering and annealing stage (green star)

The analysis of the thermal conductivity was not preformed in the RP1 samples, due to lack of qualified samples for the measurement.

4.5.4 Figure of merit

The final important property to analyse is the figure of merit, that relates all the others and it is directly connected with the potential efficiency of the material. For the samples with 5% of Nb the ZT are plotted in the Figure 51. In the set of sample with

varying sintering times (5, 10 and 20 hours) the ZT behaviour is always increasing with the temperature, showing the best values for the middle sample, where the ZT is equal to 0,12 at 970 K. The samples annealed for different times (1 minute, 10 and 20 hours) present the behaviour similar to the electric conductivity, where an initial increase is followed by a decrease at higher temperatures. In this case, the best value is once again in the middle sample, reaching a value of 0.005 at 970 K. The final sample with smaller precursor powders shows high ZT values, equal to 0,11.

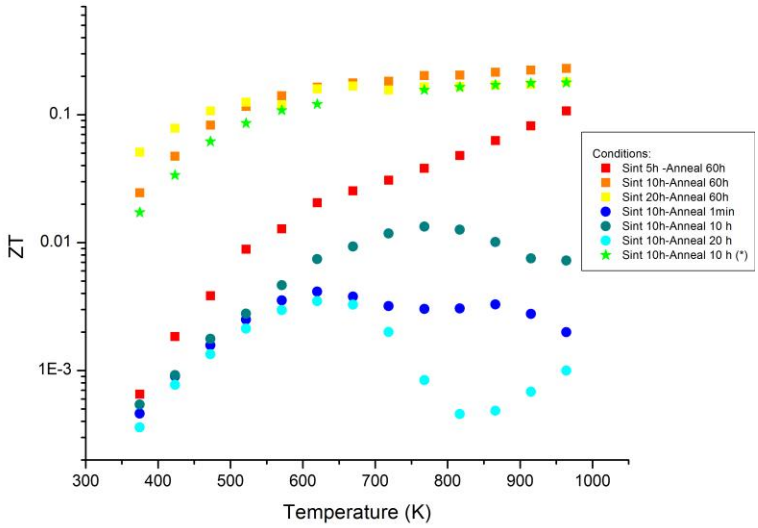

Figure 51 - Variation of the Figure of Merit with the temperature for 5% Nb doped $SrTiO_3$. Variation of the sintering time, 5, 10 and 20 hours, for a constant annealing time, 60 hours (reddish squares). Variation of the annealing time, 1 minute, 10 and 20 hours, for a constant sintering time, 10 hours (bluish points). Sample prepared with fine-grained powders for 10 hours of sintering and annealing stage (green star)

20% doped samples have the figure of merit represented in the Figure 52, where is visible an increasing dependence with the temperature. The samples with a variation in the sintering time present higher ZT values in samples sintered for less time, reaching a final value of 0,17. While the samples, where the annealing time was modified, show a higher ZT value in the sample annealed for 20 hours, obtaining a ZT value of 0,21 at 970K. The variation in precursor powder produced the sample with the highest ZT value of 0,44. A value as high as this one has not been reported before.

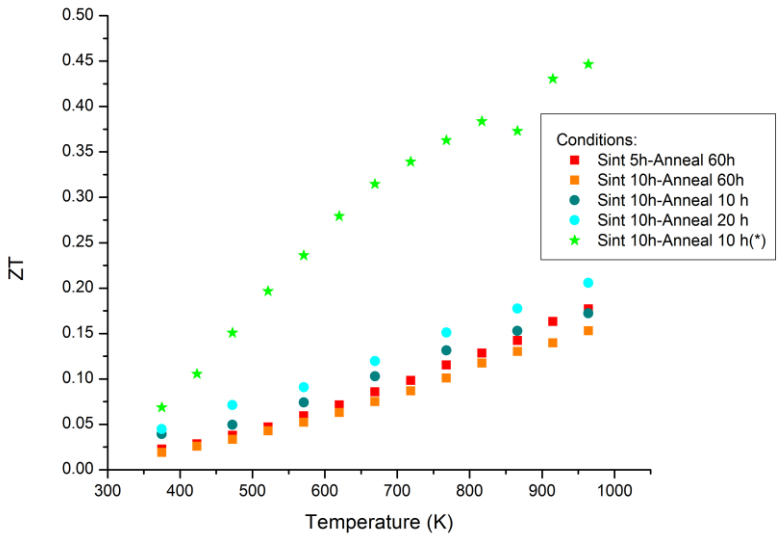

Figure 52- Variation of the Figure of Merit with the temperature for 20% Nb doped $SrTiO_3$. Variation of the sintering time, 5 and 10 hours, for a constant annealing time, 60 hours (reddish squares). Variation of the annealing time, 10 and 20 hours, for a constant sintering time, 10 hours (bluish points). Sample prepared with fine-grained powders for 10 hours of sintering and annealing stage (green star)

CHAPTER 5

Discussion

5. Discussion

The powder preparation and reduction of particle size was the primary step for the production of strontium titanate dense ceramic. After the calcination process, the structure of the powders showed variations in chemical composition, with the presence of several phases in both $SrTiO_3$ and RP1. Nevertheless, the monophasic composition, within the device resolution, was subsequently obtained in the sintering process, in an air atmosphere for $SrTiO_3$ samples and argon atmosphere for RP. This atmosphere difference between the two compositions can be explained by the instability of RP with the presence of oxygen in atmosphere. Other oxides based on Sr, Ti, and Nb appeared since the correct stoichiometry could be achieved by the incorporation of atmospheric oxygen. In the $SrTiO_3$ case, this situation would not occur due to the higher stability in an oxygen rich atmosphere. A more deep analysis can be performed by TEM to identify possible secondary phases, undetectable in XRD. The literature also reports the use of non-monophasic precursor powder for the preparation of strontium titanate ceramics[37]. The stability of the monophasic RP was not achieved in all the sintered ceramics, since secondary phases were detected in several samples, even with the maintenance of the sintering conditions. The presence of secondary phases in the RP structures is coherent with the literature, where the RP1 is reported to be highly unstable when compare with other RP phases (n=2,3)[31].

The reduction of the particle size by ball milling displayed a direct relation with the time of the process. The longer milled trials show an average particle size smaller than the shorter trials. This relation is easily explained, since the probability of a particle break increase with the time passed in the milling process No agglomeration process and presence of other phases were obtained with the used of low velocities (300 rpm). The increasing time in the milling process contributes for a decreasing in the average particle size of the powders caused by a modification of the bimodal distribution of the particles. In the first distribution, the amount of particles tends to increase in number while the second peak suffers a reduction in number of particle and shift in maximum location, being this one reduced. The average particle size tended to a limit value that had no substantial

differences after 72 hours. The final particle size distribution preserved the bimodal aspect, presenting one peak around the 200nm and the other in the 1 μm range.

The separation of the two distributions was efficiently preformed by centrifugation and filtration. The yield of finer powder obtained was around 10%, with a total or quasi-total elimination of the micron-range particles.

The introduction of Niobium in the $SrTiO_3$ structure leads to an increase of the lattice parameter originating a growth on the cell volume. This situation is a consequence of the larger ionic radius of Nb^{+5} (64.0pm) when compared with the Ti^{+4} ionic radius (60.5 pm) and indicates the incorporation of Nb in the perovskite lattice. However, the amount of Niobium inserted on the structure is additionally responsible for an increase of the mass inside a unit cell. Since the atomic mass of Nb^{+5} (92.91u) is higher than the atomic mass of Ti^{+4} (47.87u), the mass inside the cell is larger than in an undoped $SrTiO_3$. In all the compositions, the mass variation is substantial higher than the volume increase, resulting in a higher density.

The relative densities obtained are higher than 90% in the majority of the cases, showing the possibility of producing dense and heavily Nb doped $SrTiO_3$. In both STO compositions, the density increases with the sintering and annealing time, explained by longer densification periods contributing to the closure of pores. The samples produced with fine-grained powders present higher density values than the comparable ones produced with coarser powders. In the RP case, the densities presented were not higher than 95%, with a visible instability for longer annealing treatments. This situation might be explained by the formation of secondary phases, producing variation of the density of the material.

The grain growth for the less doped samples of $SrTiO_3$ is directly dependent on the sintering and annealing time, with coalescence of grains caused by longer time. Nevertheless, the samples with smaller precursor powder particle-size may have a faster grain growth than the rest of the samples. The grain size is larger when compared with samples with coarser powders and the same thermal treatments durations, evidencing a rapider grain growth.

In the highly doped samples, the grain growth in the sintering stage is normal, with a direct dependence with the time. However, in the annealing stage the grain growth seems

to occur by the formation of islands/regions where grains coalesce rapidly. While these islands are increasing in number and size, other regions maintain the finer grains. The growth presents to be abnormal and inhomogeneous, possibly caused by the relation between the N_2/H_2 atmosphere and the dopant presence, modifying the grain boundary mobility of the material. Since this growth behaviour is not visible in the lower doped samples, the high amount of niobium combined with the low oxygen pressure can trigger this growth mechanism, changing completely the microstructure of the material. Moreover, the creation of defects in the interior of the grains can be a supplementary mechanism for this type of grain growth. On the sample produced with finer powders, larger isolated grains are visible, in the 40 µm range, situation not detected in the sintered samples before the annealing treatment, supporting the evidence of an abnormal grain growth in the N_2/H_2 atmosphere for the highly doped pellets. Since these larger grains present higher amounts of Nb content when compared with the finer grains, the chemical differences between grains may be other possible explanation for the growth mechanism. Some studies also reports the abnormal grain growth of Nb doped $SrTiO_3$ samples, depending on the concentration of dopant and sintering atmosphere[47,60]. Further analysis of the grain boundary using TEM can provide a better understanding of this grain growth.

The observation of the grains in the RP1 samples was not achieved clearly, being impossible to preform a statistical analysis of the grains dimensions. Problems in the etching procedure were the cause for this situation.

On the thermoelectric properties, the initial increasing of the electric conductivity with the temperature on the 5% Nb doped samples can be attributed to the rising of intrinsic electron concentration with the temperature, followed by a decrease for higher temperatures created by the reduction of the carriers' mobility, defined as a degenerate semiconductor behaviour. This last explanation is also the reason for the constant reduction of σ in the highly doped case (20% Nb). This behaviour is usually observed for Niobium doped $SrTiO_3$[42]. The variation of conductivity in samples with the same composition might be attributed to three properties: annealing time, grain size and density. In the less doped samples, the samples annealed for longer periods, 60 hours, show the highest σ values. The reason for this behaviour of the samples is intrinsically connected to the time in the reduction period, which increases the oxygen vacancies, enhancing the electrons concentration. In this group, the one sintered for longer period, which presents higher

density and grain size, shows higher values of electric conductivity. Additionally, the sample with different precursor powders also presents a high conductivity value, possibly linked to the high relative density, despite the reduced annealing time and consequent small grain size.

The relation between microstructure properties and electric conductivity in the highly doped samples is unclear, since no trend is visible. The highest values are present in samples with higher (96,70% and 97,8%) and lower (91%) density, while in the grain size they also present (2,28 μm, 8 μm and 22,7 μm) is varied. Additionally, a relation with the annealing time is not simple since the sample with the highest σ was annealed for only 10 hours. This sample was produced with fine-grained powders and the explanation behind the electric behaviour might be attributed to the presence of large grains with higher Nb content, resulting in an increasing electric conductivity. The mechanism behind this enhancement is still unexplained. The electric conductivity values at high temperature are comparable with the studies previously analysed[17], for the 20% Nb doped samples, where the values vary from 200 to 300 $S.cm^{-1}$.

On the RP1 samples, the high resistivity hindered the continuation of a thermoelectric study, excluding this Ruddlesden-popper structure for TE applications, considering the processing characteristics used.

In the Seebeck coefficient results, the difference between the samples with different niobium content is connected with the concentration of charge carriers in each composition. Since the Seebeck coefficient is inversely dependent on the charge concentration and the high-doped sample contains a higher concentration of electrons, lower absolute value of Seebeck coefficient are observed. It is important to refer the lowest *S* value is reported on the sample annealed for less time (1minute), what stresses the importance of the electrons concentration. This sample also shows the lower σ values, supporting the evidence of lower electron concentration. In this case, the charge carrier's concentration is lower, due to short reduction time and consequent less oxygen vacancies production, reducing the creation of electronic defects on the material. The variations with sintering and annealing time are unclear, being difficult to correlate with the density or grain size. However, the samples produced with fine-coarse powders have in both compositions the lower *S* than the comparable samples. This effect has no explanation yet,

however, the literature reports increasing values of *S* with the reduction of the grain size[53], explained by the increasing volume fraction of the grain boundaries, in undoped $SrTiO_3$.

On the thermal conductivity, the variation with the temperature is decreasing, which is similar to what is reported by the literature[1]. Between samples with the same composition, the differences are a effect of the different densities and grain size. Since both grain size and density increase with the thermal treatments durations, the thermal conductivity presents higher values for the denser samples with larger grains. It is important to stress that the sample with lower thermal conductivity is the one that presents the low-density values (93%), less amount of dopant (5%), lower sintering time (10 hours), lower annealing time (1 minute) and consequent small grain size (0,4μm). The samples produced with fine powders present thermal conductivity values similar to the comparable samples in terms of composition and thermal treatments. The behaviour in all the samples was controlled by lattice contributions, since the electric component is drastically lower, around 0,4 $W.K^{-1}.m^{-1}$ for the sample with highest electric conductivity.

On the figure of merit, for the 5% Nb doped is evident that the longer annealing treatment results in the higher ZT values. The relation with the density and grain size is complex. In the 5% Nb case, the denser and larger grains samples present the best values for electric conduction, while on the thermal behaviour, the less dense and finer grain pellets show lower thermal conductivity. The higher ZT of 0,18 is for the pellet sintered for 10 hours and annealed for 60 hours combining both benefits from the two conductive properties. The finer powders sample has a high ZT of 0,177, reflection of the lower *S* and relatively high σ.

In the 20% doped cases, the samples with smaller grains and higher density present the highest values. The sample sintered with finer powders that present a bimodal grain size distribution provides the higher ZT of 0,44 at 970K. This value is a combination of the high absolute *S*, the high σ value and the low k in comparison with the other 20% doped samples. The combination of the two different sizes in the grain distribution might be the explanation for the values obtained. It is suggested that the smaller grains have the effect of decreasing the thermal conductivity, while the larger grains promote a higher electric conductivity, enabling the enhancement of ZT. Additionally, the effect of the Seebeck coefficient might be caused due to the increasing of grain boundaries. The value presented is higher than the maximum value currently reported in the literature of 0,37[42] at 1000K.

CHAPTER 6

Conclusions and Future work

6. Conclusions

A series of $SrTiO_3$ and RP1 dense ceramics were produced with varying grain size and densities for the analysis of the thermoelectric properties response.

The variation of the grain size with the two different $SrTiO_3$ compositions was one important aspect studied. While for 5% Nb doped samples the growth is proportional to the sintering time and annealing process, the pellets with a higher amount of Nb present a normal growth in the sintering process and an abnormal growth in the annealing stage. This factor can be attributed to the different atmospheres in the two processes (Air and H_2) and the relatively high amount of dopant (20%) in the samples.

On the electric conductivity, the dependence with the density is evident in the less doped samples, with the denser samples evidencing higher conductivity values. However, for the 20% Nb doped samples, a robust relation was not possible to be established. The Seebeck coefficient showed to be extremely dependent on the niobium content, without any evident relation with the density. However, the increase number of grain boundaries might be a factor for large absolute values of *S*. The dependence of the thermal conductivity with the grain size confirms previous studies, since the samples with smaller grains presented lower values of k for both compositions.

The sample with the highest ZT presented grains morphology with two distributions, one with 2μm grains that cover most part of the sample and some regions with 40 μm grains. The origin of this microstructure is connected with three factors: composition, initial powders morphology and H_2/N_2 atmosphere in the annealing treatment. The electric conductivity and Seebeck coefficient presented are substantially higher than the values reported in the literature, being the highest ZT reported for an Nb doped $SrTiO_3$ ceramic at 970K.

Nevertheless, further studies for the confirmation and understanding of the obtained results, specially focused on the bimodal grained samples is fundamental in order to better understand the thermoelectric dependence of Nb doped $SrTiO_3$ materials with the microstructure.

References

References

1 Koumoto, K., Wang, Y., Zhang, R., Kosuga, A. & Funahashi, R. Oxide thermoelectric materials: a nanostructuring approach. *Annual Review of Materials Research* **40**, 363-394 (2010).

2 Shakouri, A. Recent developments in semiconductor thermoelectric physics and materials. *Materials Research* **41**, 399 (2011).

3 MacDonald, D. K. C. *Thermoelectricity: an introduction to the principles*. (Dover Publications, 2006).

4 Yang, J. & Caillat, T. Thermoelectric materials for space and automotive power generation. *MRS bulletin* **31**, 224-229 (2006).

5 Tritt, T. M. Thermoelectric phenomena, materials, and applications. *Annual Review of Materials Research* **41**, 433-448 (2011).

6 Kasap, S. Thermoelectric effects in metals: thermocouples. *Canada: Department of Electrical Engineering University of Saskatchewan* (2001).

7 Nicolaou, M. C. *Thermoelectric figure of merit of degenerate and nondegenerate semiconductors*. (ProQuest, 2009).

8 Vining, C. B. An inconvenient truth about thermoelectrics. *Nature Materials* **8**, 83-85 (2009).

9 Vineis, C. J., Shakouri, A., Majumdar, A. & Kanatzidis, M. G. Nanostructured Thermoelectrics: Big Efficiency Gains from Small Features. *Advanced Materials* **22**, 3970-3980, doi:10.1002/adma.201000839 (2010).

10 Li, J.-F., Liu, W.-S., Zhao, L.-D. & Zhou, M. High-performance nanostructured thermoelectric materials. *NPG Asia Materials* **2**, 152-158 (2010).

11 Chen, Z.-G., Han, G., Yang, L., Cheng, L. & Zou, J. Nanostructured thermoelectric materials: Current research and future challenge. *Progress in Natural Science: Materials International* (2012).

12 Venkatasubramanian, R., Siivola, E., Colpitts, T. & O'quinn, B. Thin-film thermoelectric devices with high room-temperature figures of merit. *Nature* **413**, 597-602 (2001).

13 Biswas, K. *et al.* High-performance bulk thermoelectrics with all-scale hierarchical architectures. *Nature* **489**, 414-418 (2012).

14 Leonov, V., Fiorini, P., Sedky, S., Torfs, T. & Van Hoof, C. in *Solid-State Sensors, Actuators and Microsystems, 2005. Digest of Technical Papers. TRANSDUCERS '05. The 13th International Conference on.* 291-294 Vol. 291.

15 Bhatia, D., Bairagi, S., Goel, S. & Jangra, M. Pacemakers charging using body energy. *Journal of Pharmacy And Bioallied Sciences* **2**, 51 (2010).

16 Fergus, J. W. Oxide materials for high temperature thermoelectric energy conversion. *Journal of the European Ceramic Society* **32**, 525-540 (2012).

17 Ohta, S. *et al.* Large thermoelectric performance of heavily Nb-doped SrTiO3 epitaxial film at high temperature. *Applied Physics Letters* **87**, 092108-092103 (2005).

18 Choi, S.-M., Lee, K.-H., Lim, C.-H. & Seo, W.-S. Oxide-based thermoelectric power generation module using p-type Ca3Co4O9 and n-type (ZnO) 7In2O3 legs. *Energy conversion and management* **52**, 335-339 (2011).

19 Frederikse, H. P. R., Thurber, W. R. & Hosler, W. R. Electronic Transport in Strontium Titanate. *Physical Review* **134**, A442-A445 (1964).

20 Last, J. T. Infrared-Absorption Studies on Barium Titanate and Related Materials. *Physical Review* **105**, 1740-1750 (1957).

21 Bhalla, A. S., Guo, R. & Roy, R. The perovskite structure – a review of its role in ceramic science and technology. *Mat Res Innovat* **4**, 3-26, doi:10.1007/s100190000062 (2000).

22 Cowley, R. A. Lattice Dynamics and Phase Transitions of Strontium Titanate. *Physical Review* **134**, A981-A997 (1964).

23 Schooley, J. F., Hosler, W. R. & Cohen, M. L. Superconductivity in Semiconducting SrTiO3. *Physical Review Letters* **12**, 474-475 (1964).

24 Shirane, G. & Yamada, Y. Lattice-Dynamical Study of the 110°K Phase Transition in SrTiO3. *Physical Review* **177**, 858-863 (1969).

25 Müller, K. A. & Burkard, H. SrTiO3: An intrinsic quantum paraelectric below 4 K. *Physical Review B* **19**, 3593-3602 (1979).

26 Liu, H., Sun, X., Zhao, Q., Xiao, J. & Ouyang, S. The syntheses and microstructures of tabular SrTiO3 crystal. *Solid-State Electronics* **47**, 2295-2298 (2003).

27 Li, L., Zhao, J. & Gui, Z. The thermal sensitivity and dielectric properties of SrTiO3-based ceramics. *Ceramics international* **30**, 1073-1078 (2004).

28 Scott, A. W. Understanding microwaves. (1993).

29 Ohta, H. *et al.* Giant thermoelectric Seebeck coefficient of a two-dimensional electron gas in SrTiO3. *Nature Materials* **6**, 129-134 (2007).

30 Liu, J. *et al.* Enhancement of thermoelectric efficiency in oxygen-deficient Sr 1-x La x TiO 3-δ ceramics. *Applied Physics Letters* **95**, 162110-162110-162113 (2009).

31 Wang, Y. F., Lee, K. H., Ohta, H. & Koumoto, K. Fabrication and thermoelectric properties of heavily rare-earth metal-doped SrO (SrTiO3)n(n= 1, 2) ceramics. *Ceramics international* **34**, 849-852 (2008).

32 Wang, H. & Wang, C. Thermoelectric properties of Yb-doped La0.1Sr0.9TiO3ceramics at high temperature. *Ceramics international* (2012).

33 Ohta, S., Nomura, T., Ohta, H. & Koumoto, K. High-temperature carrier transport and thermoelectric properties of heavily La-or Nb-doped SrTiO3 single crystals. *Journal of Applied Physics* **97**, 034106-034106-034104 (2005).

34 Liu, J. *et al.* Synthesis and thermoelectric properties of Sr0.95La0.05TiO3− δTiO2solid solutions. *Solid State Sciences* **12**, 134-137 (2010).

35 Kikuchi, A., Okinaka, N. & Akiyama, T. A large thermoelectric figure of merit of La-doped SrTiO3 prepared by combustion synthesis with post-spark plasma sintering. *Scripta Materialia* **63**, 407-410 (2010).

36 Fukuyado, J., Narikiyo, K., Akaki, M., Kuwahara, H. & Okuda, T. Thermoelectric properties of the electron-doped perovskites Sr1− xCaxTi1− yNbyO3. *Physical Review B* **85**, 075112 (2012).

37 Ito, M. & Ohira, N. Synthesis of Y-Doped n-Type SrTiO3 Thermoelectric Oxides by Polymerized Complex Process. *Materials transactions* **49**, 1844-1847 (2008).

38 Liu, J. *et al.* Thermoelectric Properties of Dy-Doped SrTiO3 Ceramics. *Journal of Electronic Materials* **41**, 3073-3076 (2012).

39 Liu, J. *et al.* Thermoelectric properties of Sr1− x NdxTiO3ceramics. *Journal of Alloys and Compounds* **492**, L54-L56 (2010).

40 Sun, R. *et al.* Transport and thermoelectric properties of Sr 3 (Ti 0.95 R 0.05) 2 O 7 (R= Ta, Nb, W) oxides. *Journal of Applied Physics* **112**, 124904-124904-124908 (2012).

41 Kato, K. *et al.* The effect of Eu substitution on thermoelectric properties of SrTi0.8Nb0.2O3. *Journal of Applied Physics* **102**, 116107-116107-116103 (2007).

42 Ohta, S., Ohta, H. & Koumoto, K. Grain size dependence of thermoelectric performance of Nb-doped SrTiO3 polycrystals. *Nippon seramikkusu kyokai gakujutsu ronbunshi* **114**, 102-105 (2006).

43 Choi, W. S., Ohta, H., Moon, S. J., Lee, Y. S. & Noh, T. W. Dimensional crossover of polaron dynamics in Nb: SrTiO3/SrTiO3 superlattices: Possible mechanism of thermopower enhancement. *Physical Review B* **82**, 024301 (2010).

44 Sonne, M., Van Nong, N., He, Z., Pryds, N. & Linderoth, S. Improvement of Niobium Doped SrTiO3 by Nanostructuring.

45 Wang, N., He, H., Li, X., Han, L. & Zhang, C. Enhanced thermoelectric properties of Nb-doped SrTiO3polycrystalline ceramic by titanate nanotube addition. *Journal of Alloys and Compounds* **506**, 293-296 (2010).

46 Moos, R. & Hardtl, K. H. Defect Chemistry of Donor-Doped and Undoped Strontium Titanate Ceramics between 1000° and 1400° C. *Journal of the American Ceramic Society* **80**, 2549-2562 (1997).

47 Cho, S. & Johnson, P. Evolution of the microstructure of undoped and Nb-doped SrTiO3. *Journal of Materials Science* **29**, 4866-4874 (1994).

48 Lee, K. H., Wang, Y. F., Kim, S. W., Ohta, H. & Koumoto, K. Thermoelectric Properties of Ruddlesden–Popper Phase n-Type Semiconducting Oxides: La-, Nd-, and Nb-Doped Sr3Ti2O7. *International journal of applied ceramic technology* **4**, 326-331 (2007).

49 Zhou, N., Chen, G., Xian, H. & Zhang, H. Synthesis of SrO (SrTiO3)n; (n= 1, 2,∞) compounds and electronic structure analysis. *Materials Research Bulletin* **43**, 2554-2562 (2008).

50 McHale, A. *Phase Equilibria Diagrams: Phase Diagrams for Ceramists*. (American Ceramic Society, 1994).

51 Sun, R. *et al.* Preparation and thermoelectric properties of rare-earth-metal-doped SrO (SrTiO3) n oxides. *Procedia Engineering* **27**, 103-108 (2012).

52 Zhang, R.-z., Hu, X.-y., Guo, P. & Wang, C.-l. Thermoelectric transport coefficients of n-doped CaTiO3, SrTiO3 and BaTiO3: A theoretical study. *Physica B: Condensed Matter* **407**, 1114-1118 (2012).

53 Gregori, G., Heinze, S., Lupetin, P., Habermeier, H.-U. & Maier, J. Seebeck coefficient and electrical conductivity of mesoscopic nanocrystalline SrTiO3. *Journal of Materials Science* **48**, 2790-2796 (2013).

54 Gregori, G., Lupetin, P. & Maier, J. Huge Electrical Conductivity Changes in SrTiO3 upon Reduction of the Grain Size to the Nanoscale. *ECS Transactions* **45**, 19-24 (2012).

55 Lingner, J., Letz, M. & Jakob, G. SrTiO3 glass–ceramics as oxide thermoelectrics. *Journal of Materials Science* **48**, 2812-2816 (2013).

56 German, R. M., Messing, G. L. & Cornwall, R. G. *Sintering Technology*. (Marcel Dekker, 1996).

57 Tanaka, H., Yamamoto, A., Shimoyama, J.-i., Ogino, H. & Kishio, K. Strongly connected ex situ MgB2 polycrystalline bulks fabricated by solid-state self-sintering. *Superconductor Science and Technology* **25**, 115022 (2012).

58 Chung, S. Y. & Kang, S. J. L. Effect of dislocations on grain growth in strontium titanate. *Journal of the American Ceramic Society* **83**, 2828-2832 (2000).

59 Cho, S. G. & Johnson, P. F. Evolution of the microstructure of undoped and Nb-doped SrTiO3. *Journal of Materials Science* **29**, 4866-4874, doi:10.1007/bf00356536 (1994).

60 Chung, S.-Y., Kang, S.-J. L. & Dravid, V. P. Effect of Sintering Atmosphere on Grain Boundary Segregation and Grain Growth in Niobium-Doped SrTiO3. *Journal of the American Ceramic Society* **85**, 2805-2810, doi:10.1111/j.1151-2916.2002.tb00532.x (2002).

61 Coulter, L. Series Product Manual. *USA, Miami, Coulter Corporation*, 14 (1994).

62 Marra, W., Eisenberger, P. & Cho, A. X-ray total-external-reflection–Bragg diffraction: A structural study of the GaAs-Al interface. *Journal of Applied Physics* **50**, 6927-6933 (1979).

63 Pratten, N. The precise measurement of the density of small samples. *Journal of Materials Science* **16**, 1737-1747 (1981).

64 Hecht, E. *Optics*. (Pearson Education, 2008).

65 Goldstein, J. *et al. Scanning electron microscopy and X-ray microanalysis*. (Springer, 2003).

66 A. Mayolett, H. B., H. Wang, J. Konig, J. Semwiratne, L. Chen, S. Bai, T. Tritt, W. Porter. Thermoelectric Materials for Waste Heat Recovery: An International Collaboration for Transportation Applications. (2011).

67 Ulvac-Riko, I. *Seebeck Coefficient and Electric Resistance Measuring-System*, <http://www.ccrprocessproducts.com/media/catalog/customfield/ZEM-3_Product_Data_Sheet.pdf>

68 Oliviera, E. P., Silva, Zaqueu Ernesto, Silva, Cristiane Kelly F. da. The flash method to the measurement of the thermal properties of yogurt. *20th International Congress of Mechanical Engineering* (2009).

69 Hatakeyama, T. & Quinn, F. *Fundamentals and Applications to Polymer Science*. (Thermal Analysis, 1994).

Appendices

Appendices

Maximum power

The maximum power for the thermoelectric generation is achieved with the following considerations:

$$P = I^2 R_L;\ I = \frac{S\Delta T}{R+R_L}$$

$$P = \left(\frac{S\Delta T}{R+R_L}\right)^2 R_L$$

For maximization:

$$\frac{dP}{dR_L} = (S\Delta T)^2 \frac{(R+R_L)^2 - 2R_L(R+R_L)}{(R+R_L)^4}$$

$$\frac{dP}{dR_L} = (S\Delta T)^2 \frac{R^2 + 2RR_L + R_L^2 - 2R_L R - 2R_L^2}{(R+R_L)^4}$$

$$\frac{dP}{dR_L} = (S\Delta T)^2 \frac{R^2 - R_L^2}{(R+R_L)^4}$$

$$\frac{dP}{dR_L} = (S\Delta T)^2 \frac{(R-R_L)}{(R+R_L)^3}$$

If we consider:

$$\frac{dP}{dR_L} = 0$$

$$R = R_L$$

Maximum efficiency - Figure of merit determination

Considering the efficiency of the electric generator:

$$\eta = \frac{P}{\dot{Q}} = \frac{I^2 R_L}{ST_1 + K\Delta T - \frac{I^2 R}{2}}$$

Considering the electric current produced by the thermoelectric part and the ratio of resistances:

$$I = \frac{S\Delta T}{R+R_L}$$

$$x = \frac{R_L}{R}$$

$$\eta = \frac{\left(\frac{S\Delta T}{R(1+x)}\right)^2 xR}{\frac{S\Delta T}{R(1+x)} ST_1 + K\Delta T - \left(\frac{S\Delta T}{R(1+x)}\right)^2 \frac{R}{2}}$$

$$\eta = \frac{\frac{S^2\Delta T^2}{R(1+x)}}{\frac{S^2\Delta T T_1}{R(1+x)}} \quad \frac{\frac{x}{x+1}}{1 + \frac{KR(1+x)}{S^2 T_1} - \frac{\Delta T}{2T_1(1+x)}}$$

$$\eta = \frac{\Delta T}{T_1} \quad \frac{\frac{x}{x+1}}{1 + \frac{KR(1+x)}{S^2 T_1} - \frac{\Delta T}{2T_1(1+x)}}$$

The only terms that are independent from temperature and x are in the same term that is substituted to:

$$Z = \frac{S^2}{KR} = \frac{S^2\sigma}{k}$$

where k is the thermal conductivity and σ is the electrical conductivity. The efficiency is now express as:

$$\eta = \frac{\Delta T}{T_1} \quad \frac{\frac{x}{x+1}}{1 + \frac{(1+x)}{ZT_1} - \frac{\Delta T}{2T_1(1+x)}}$$

The optimization of the efficiency occurs when:

$$\frac{d\eta}{dx} = 0$$

$$\frac{d\eta}{dx} = \frac{1-x^2}{ZT_1} - \frac{\Delta T}{2T_1} + 1$$

Considering an average temperature between the source and sink heat:

$$T_m = \frac{T_1 + T_2}{2} = \frac{2T_1 - \Delta T}{2}$$

$$\Delta T = 2T_1 - T_m$$

We can define:

$$\frac{d\eta}{dx} = \frac{1-x^2}{ZT_1} + \frac{T_m}{T_1}$$

And as we are maximizing n:

$$\frac{1-x^2}{ZT_1}+\frac{T_m}{T_1}=0$$
$$x=\frac{R_L}{R}=\sqrt{ZT_m+1}$$

and the efficiency is equal to:

$$\eta=\frac{\Delta T}{T_1}\quad\frac{\sqrt{1+\ \mathrm{ZT}}-1}{\sqrt{1+\ \mathrm{ZT}}+\frac{\mathrm{T_2}}{\mathrm{T_1}}}$$